Karlsruhe Institute of Technology

Institute of Fluid Mechanics

Numerical Simulation of the Cutting of a Rising Bubble by a Horizontal Cylinder

Numerische Simulation von Zerteilung einer steigenden Blase durch einen Horizontalen Zylinder

Master Thesis of

Shuo Wang

At the Department of Mechanical Engineering,
Institute of Fluid Mechanics

Advisors: Prof. Dr.-Ing. Bettina Frohnapfel
Dr.-Ing. Martin Wörner

Duration: July 2018 – January 2019

I declare that I have developed and written the enclosed thesis completely by myself, and have not used sources or means without declaration in the text.

Karlsruhe, 31. 01. 2019

.....

(**Shuo Wang**)

Abstract

The study is devoted to the numerical simulation of bubble interaction with horizontal cylinder. The phase field method is used. It is firstly validated for free bubble rising in a planar domain. The numerical result is consistent with benchmark from literature. The numerical method is applied to the study of bubble behavior of cutting by solid cylinder under different conditions. Planar simulation is performed to investigate the influence of different bubble diameter (4.57 mm-7.8 mm) and contact angle (60°-120°). The results are in qualitative consistence with experiment. 3D simulations are made for further quantitative investigation. To reduce the calculation cost, adaptive refinement is discussed and applied in the discretization of the domain. 3D simulation shows the deformation by the cutting comprehensively and confirms the conclusion of the previous experiment investigation that the cylinder is completely wetted by the cutting. At last, the behavior of the satellite bubble under different conditions is studied. However, the mesh resolution is turns out to to be not enough for a precise description of this phenomena.

Acknowledgement

First and foremost, I would like to deeply appreciate Dr. Martin Wörner, my scientific advisor. With his immense knowledge and patience, Martin has provided invaluable scientific advice and constant encouragement throughout all my master thesis.

I own many thanks to Dr. Xuan Cai for his original numerical set-up and more importantly, the experience on the installation and running of the solver code as well as the usage of the cluster that he shared with me at the beginning stage of my master thesis.

I am deeply grateful to M.Sc. Andrea Schillaci for his great contribution to the application of new version of *phaseFieldFoam* and especially the application of adaptive mesh refinement and besides, the daily helps and pleasant discussions on scientific/non-scientific topics in office or during lunch time.

I own many thanks to Dr. Klostermann and Prof. R. Schwarze, for their detailed suggestion on the Hysing's benchmark.

Last but not the least, I thank Prof. B. Frohnapfel for the possibility to perform this master thesis at ISTM.

Contents

1. Introduction

Multi-phase reactors are widely applied in chemistry, petroleum chemical-biological industry for production of petroleum based fuel or other material of chemical and pharmaceutical usage [15]. Fixed bed reactors and bubble column reactors are firstly applied in this process, which are to be improved due to problems of backmixing of the fluid and bubble fusion. The bubble fusion in bubble column reactors leads to the decrease of gas-liquid interface area, which is essential for enhancement of mass transfer.
Inner structure, for example the structured package [21] and grid mesh in bubble column reactors, is developed to overcome this limitation, which serve to cut large bubbles in to smaller ones and thus increase the specific multi-phase mass transfer area. Structured geometry in multiphase reactor shows higher efficiency than random located packages due to effective radial mixing properties [27]. Besides the cut of the bubbles, this structure leads to also resurfacing. Working with catalytic layered grid mesh structure, the structured geometry an increase the gas-fluid mass transfer for 10 times [17].

(a) Structured packages (POCS) [21].

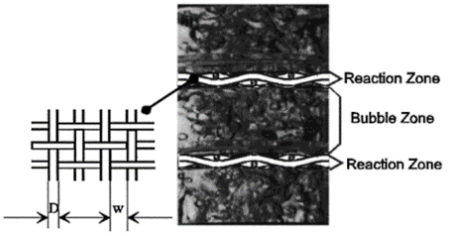

(b) catalytic layered tissue [17].

Figure 1.1: Example of inner structure

Instead of structured wire mesh, single cylinder is studied to understand the most under-

lying physics in the process of bubble cutting. Comprehensive understanding influence of the relevant parameters, for instance, bubble size, physical parameter of the liquid and the cylinder surface material is of importance to optimize the design and application of this kind of reactors. Several experimental and numerical investigation have been made on the bubble cutting. Baltussen et al. [2] made numerical simulations with VOF method on the interaction between a bubble and wire mesh and collected the first impression of bubble cutting. The bubble behavior differs with different Eötvos number. The wire mesh gets partially dewetted in all the under all simulation conditions. Segers [33] made experimental investigation on the structured packages, in which influence of different bubble diameters, fluid viscosity and cylinder diameter are discussed. The result showed that the bubble diameters and fluid viscosity affect the behavior of the bubble whereas the cylinder diameter makes little difference. Segers [33] gave also a criterion, whether the bubble will be cut into smaller bubbles, in stead of slipping from one side of the cylinder or being attached on the surface of the cylinder. Cai et al. [8] performed numerical simulations based on phase field method on the influence of wettability of the cylinder material. The results showed significant difference between different contact angle. However, this difference could not be observed in experiment with very similar properties performed by Rohlfs [30]. In the experiment thin liquid film covered the whole surface of the solid cylinder, which at the same time isolated the bubble from the solid cylinder. The liquid film is believed to be essential to the independence on the wettability of the surface of the cylinder, since contact angle is typically considered in the problem of contact line. The main purpose of the thesis is to perform numerical simulations to provide details of the deformation of during a bubble cutting process and especially the behavior of liquid film.

The thickness of the liquid film is much smaller than the bubble diameter and precise predictions of the liquid film requires hence better resolution of mesh. Mesh resolution in the previous investigation [8] were limited by calculation capability. This dilemma can be possibly solved by adaptive refinement method available in a later version of phase field method based solver *phaseFieldFoam*4.0, which is used in this thesis. The thesis is organized as follows:

Chapter 2 introduces the physical mathematical fundamentals. Necessary physical facts of bubble rising and cutting will be explained in detail. Furthermore, fundamentals of phase field method and the numerical approach in *phaseFieldFoam* is presented. A short introduction of AMR method is given in the end of the chapter.

Chapter 3 validates the numerical method by comparison with free bubble rising problem. The reference is selected from benchmark in the literature. Velocity evolution is validated with different numerical parameter at first and the comparison of terminal shape serves a further validation.

Chapter 4 introduces the simulation of bubble cutting. Axisymmetric simulation is performed to determine the domain and other numerical parameter for following simulations. Simulations are made in planar domain firstly for preliminary results and to investigate the influence of wettability of cylinder surface. Finally, the result of 3D simulation is given. Discussion of the result is focused on three topics: the global 3D deformation, the liquid film and behavior of satellite bubble.

Chapter 5 summarizes the whole work and gives the outlook of the future investigation. The numerical simulation facilities to provide comprehensive understanding of the deformation of the bubble by interaction with solid cylinder.

2. Fundamentals

The bubble cutting phenomena is investigated by numerical simulation. The related phenomena in terms of wetting, bubble rising and bubble-solid interaction are here introduced. The mathematical formulation, which is based on coupling of Navier-Stokes equation and phase-field model is then presented.

2.1 Physical Fundamentals

A typical single bubble cutting process can be divided into two stages: the bubble rises and then interacts with the solid barrier. Physical description of both stages is presented here.

2.1.1 Theoretical Description of Bubble Rising

A variety of characteristic numbers determine the behavior of a rising bubble. Before the introduction of the characteristic numbers the equivalent diameter of the bubble is given here and serves as the characteristic length for at least the global consideration of the bubble shape. The equivalent bubble diameter is the diameter of a sphere with the same volume of the bubble V_b:

$$d_{\mathrm{eq}} = \sqrt[3]{\frac{6 \cdot V_b}{\pi}} \tag{2.1}$$

The Reynolds number Re is the ratio of inertia to viscous forces and plays an important role to determine the bubble rising velocity. It is defined by surrounding fluids density ρ_{L}, bubble velocity u_{b},the equivalent diameter d_{eq} and the dynamic viscosity of the liquid η_l:

$$Re = \frac{\rho_{\mathrm{L}} \cdot u_{\mathrm{b}} \cdot d_{\mathrm{eq}}}{\mu_{\mathrm{L}}} \tag{2.2}$$

The Eötvös number is the ratio of buoyancy to surface tension forces. It is defined by the density difference between the liquid and gas $\Delta\rho = \rho_{\mathrm{L}} - \rho_G$, gravity g, equivalent diameter d_{eq} and surface tension σ:

$$Eo = \frac{\Delta\rho \cdot g \cdot d_{\mathrm{eq}}^2}{\sigma} \tag{2.3}$$

The property of the fluid is characterized by Morton number, which is defined as:

$$Mo = \frac{\Delta\rho \cdot g \cdot \mu_{\mathrm{l}}^4}{\sigma^3 \cdot \rho_{\mathrm{L}}^2} \tag{2.4}$$

The bubble shape is determined by Eötovös number and Morton number [16].
The Weber number is important in the interaction between the bubble and the cylinder. It builds the relation between the kinetic energy and surface tension:

$$We = \frac{\rho_{\mathrm{L}} \cdot u_{\mathrm{b}}^2 \cdot d_{\mathrm{eq}}}{\sigma} \tag{2.5}$$

The two domineering factors, buoyancy force and drag force work against each other in the processing of bubble rising. The bubble accelerates when buoyancy over weights resistance whereas decelerates when resistance is over buoyancy. Clift et al. [29] found that the bubble velocity and drag force F_D is relevant to the Reynolds and Eötovös number. The buoyancy force F_B is defined by the density difference between the bubble and the surrounding fluid $\Delta\rho$, the gravity g, and the bubble volume V_b:

$$F_{\mathrm{B}} = g \cdot \Delta\rho \cdot V_b \tag{2.6}$$

In the researched case, the bubble is released from static state and the resistance is at the beginning considerably small. In the acceleration phase the resistance also increases until balance with buoyancy, which is consider constant, is attained.

Bubble shapes can be categorized typically into 3 kinds:
a.) Spherical
b.) Elliptical
c.) Ellipsoidal cap

(a) Spherical (b) Elliptical (c) Ellipsoidal cap

Figure 2.1: Bubble shape [30]

The small bubbles have spherical shapes. In this case surface tension determines the shape tends to keep the minimum surface area. Shapes of larger bubbles are elliptical under influence of stronger buoyancy and and resistance. For the largest bubbles, the surface tension can be almost ignored compared with buoyancy and resistance.

The shape of bubble are determined by Reynolds and Eötvös number. The relation of the bubble shapes and the Reynolds and Eötvös number are shown in figure 2.2. The curves are the iso-curves in log form of Morton number. The red curve shows the region investigated by Rohlfs [30], where the influence of surface tension is stronger than viscosity, and the bubbles shows ,therefore, elliptical shape.

The aspect ratio A_{r}, defined as

$$A_{\mathrm{r}} = \frac{h}{w} \tag{2.7}$$

serves to describe the shape of the bubble, where the height h and the width w of the bubble are typical as shown in figure 2.3. The value of aspect ratio is 1 for perfect spherical shape and the smaller the aspect ratio is, the stronger the bubble deforms. Aoyama et al. [1]

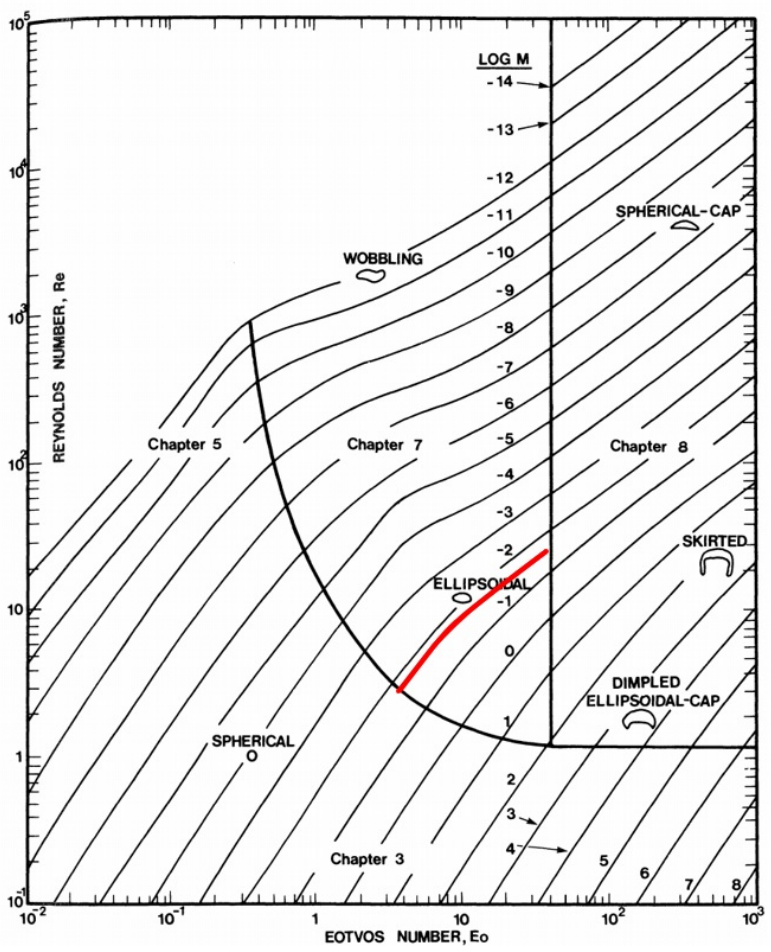

Figure 2.2: Characteristics of Bubble in Gravity Field [29]

established a correlation for the aspect ratio of the bubble as function of Reynolds and Eötvös number.

$$A_r = \frac{1}{(1 + 0.016 \cdot Eo^{1.12} \cdot Re)^{0.388}} \tag{2.8}$$

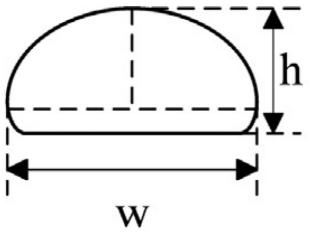

Figure 2.3: Aspect ratio of a bubble [24]

2.1.2 Bubble-Cylinder Interaction

The behavior of a bubble cut by wire mesh or single cylinder is under influence of many factors at different stages. The exact hydrodynamic process of bubble break up is still to find.

Baltussen et al. [2] made an investigation on the interaction between a single bubble

and wire mesh with combined VOF-IB method. The result shows that the single bubble will keep attached to the wire mesh when the bubble is small and/or the inter-space of the wire mesh is small, whereas larger bubble, in which case $Eo > 4$, will rise through the wire mesh. The size of one single wire or the diameter of the cylinder as well as the structure of the mesh will then impose its influence on the behavior of the bubble. All the simulations show partial dewetting process on the surface of the cylinder, which means, that the wettability of the cylinder material can be also a factor that affects the bubble cutting behavior.

Segers [33] made research based on another experiment, where the bubble position, cylinder diameter, bubble size and properties of the fluids are investigated. The results show that the fluid with smaller viscosity leads to significantly larger possibility of bubble break up. The reason is, under smaller Reynolds number as a result of smaller viscosity, the spherical bubble turns to be in elliptical shape and therefore increase the contact surface area on the cylinder. However, the influence of cylinder material wettability has not been investigated.

2.1.3 Wetting Phenomenon

Wetting is the phenomenon of a liquid to maintain contact with a solid surface. It describes how a liquid comes into contact with solid surface [20]. Wetting phenomenon is of widespread existence in the nature and industrial application. A good example of wetting in the nature is the lotus effect. As shown in the figure 2.4, the rain droplet stay in spherical shape to minimize the surface of interaction with the leaves due to special microscopic texture of the leaves. Wetting phenomenon appear also in applications such as inject printing, digital printing, coating and so on. A comprehensive understanding of this phenomenon is therefore of importance [38].

Figure 2.4: Lotus effect. Taken from [3]

Wettability is relevant to the surface energy of the material. Low energy surface tends to have more interaction with liquid whereas surface with higher energy shows a liquid repellent feature.

The notion of wettability is first mentioned by Young in 1805 [40]. In order to quantify the wetting phenomenon, the concept contact angle was proposed. It indicates the angle between the surface and tangent of the edge of the droplet. Young's equation is derived from the mechanic equilibrium of the three interfacial tensions:

$$\gamma_{SV} = \gamma_{LV} \cdot \cos\theta + \gamma_{SL} \tag{2.9}$$

Figure 2.5: Young's equation [23]

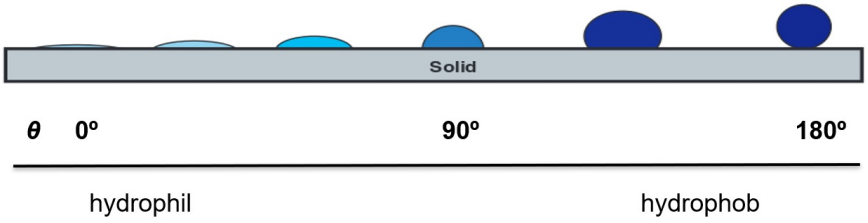

Figure 2.6: Contact angle[23]

Therein γ_{SV}, γ_{LV},and γ_{SL} are gas-solid,gas-liquid and liquid-solid interracial tension, respectively. It can be concluded from Young's equation that the contact angle is determined by the three interfacial tensions.

A contact angle with 0° means that the surface is completely wetted. Partial wetting appears when θ is smaller than 90°. The surface can be hardly wetted in $\theta >$ 90° Finally, material is called ultra hydrophobic is contact angle is typically higher than 150° as shown on the right side of figure 2.6.

Static contact angle is according to equation (2.9) purely dependent on the physical properties of the material. The equilibrium contact angle varies form from the advancing contact angle θ_A to the receding contact angle θ_R, which are the maximum and minimum values of contact angle, respectively [34]. This contact angle hysteresis includes the influence of surface roughness and heterogeneity of the surface indicates the difference of solid-interfacial tension by the motion of the interface [22]. Since all the surface are assumed to be ideally smooth, chemically homogeneous, rigid and inert in this article and no "contact line" motion is expected in this thesis, the influence of contact angle hysteresis can be neglected.

2.1.4 Wettability and Bubble Cutting

The influence of wettability should be included in the consideration of the interaction between air bubbles and solider in fluid surroundings.

Cai et al. [8] investigated the influence different contact on the cutting behavior of a rising bubble by a horizontal cylinder with numerical simulation. The simulation was composed under $Re = 9.85$, $Eo = 19.6$. The diameter of cylinder is 3.1 mm and the bubble diameter is 9.14 mm. The result shows that contact angle θ imposed influence both on the bubble cutting behavior and the bubble shape. Smaller contact angle will enhance the possibility od cutting and thus increase the mass transfer for industrial application. As shown in figure 2.7, the interaction between a bubble and a cylinder can be categorized into three species for different wettability [8, 2]:

a) Slip over without cut

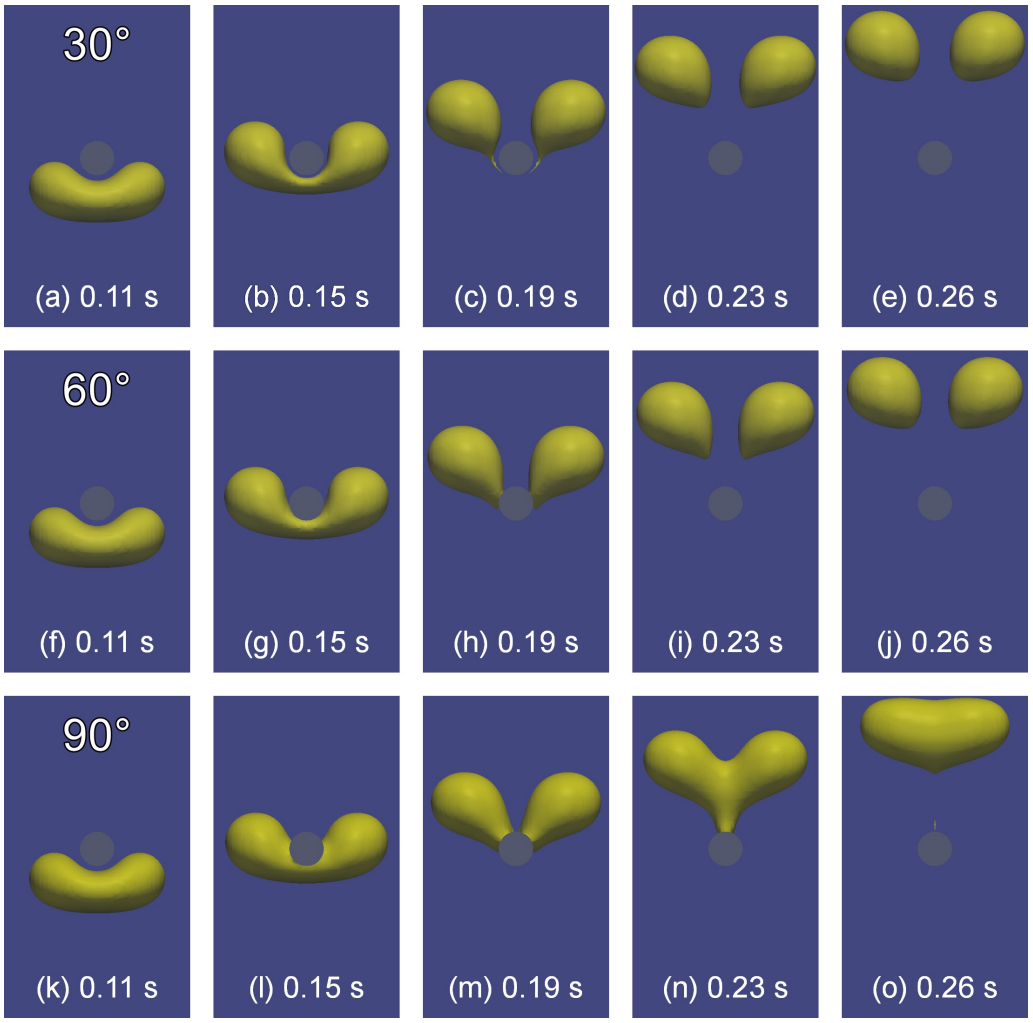

Figure 2.7: Simulation of bubble cutting by a cylinder, composed by Cai et al.[8](top row θ= 30°, middle row θ= 60°, bottom row θ= 90°)

Smaller bubbles with spherical shape tend to be attached to the bottom of the cylinder or slip away driven by the buoyancy [2]. Spherical shape leads to relatively smaller contact surface area with the cylinder [33] and the bubble will not break up because the surface tension weights over the other forces and keep the bubble complete.

b) Cut and generation of daughter bubbles
Larger bubbles with elliptical or cap shape and larger rising velocity will be cut by the cylinder into two daughter bubbles. The critical value is usually $1<We<5$ and higher Weber number than the critical value will lead to break-up [33]. The critical Weber number will decrease with increasing viscosity, since larger viscosity will reduce the kinetic energy and therefore a smaller Weber number [33].

c) Enclosure of the cylinder and re-coalescence
Cai et al. [8] observed in numerical investigation that a larger bubble is cut into two parts by cylinde rwith large contact angle, the two daughter bubble keep attached to the cylinder and at the same time slide to the upper part of the cylinder where the two daughter bubbles meet and reconnect to each other. This phenomena is, however, not confirmed in experiment investigations [30].

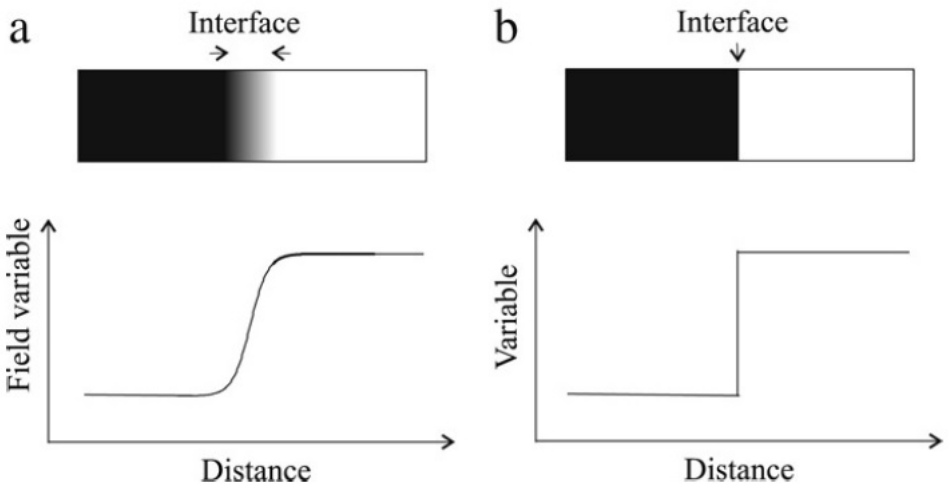

Figure 2.8: Diffusive and sharp interface [25]

2.2 Mathematical Fundamentals

The numerical investigation of bubble cutting is based on phase field method. On the contrary to the conventional numerical approach, which must deal with the conflict between the no-slip boundary condition on the wall and the moving contact line, the phase field phase field method resolve this paradox by a application of diffusive mechanism [19] of interface and moreover, it is easier to handle topology transactions of interface (e.g. bubble break up), which is common in multi-phase flow. The phase field method and the governing equation are introduced in this section. The numerical scheme is included at the end of this section.

2.2.1 Cahn-Hilliard-Navier-Stokes Equations

The phase field method is based on the assumption of interface with finite-small interface width. The movement and deformation can be calculated with Euler method [19]. The interfacial forces is modeled with chemical potential and is included in the Navier-Stokes equation for multi-phase flow. Figure 2.8 shows the difference of diffusive and sharp interface model. The distribution of liquid and gas phase is indicated by order parameter C in phase-field method; C is also called phase-field variable [39]. The value of C is $C_{\mathrm{L}} = 1$ for liquid phase and $C_{\mathrm{G}} = -1$ for gas phase. The order parameter C undergoes a rapid but smooth increase or decrease across the interface and the mixing density can be then derived by C [4, 44]:

$$f = \frac{1}{2}\lambda|\nabla C|^2 + \frac{\lambda}{4\epsilon^2}(C^2-1)^2 \tag{2.10}$$

where the first term is the gradient energy and the second term is the bulk energy. λ is free energy density parameter and ϵ is the capillary width, which determines the interface thickness. The mixing energy of the system can be then expressed as:

$$F = \int_V f \mathrm{d}V \tag{2.11}$$

where V is the volume of the domain of the system. The chemical potential ϕ is defined as the variational derivative of the mixing energy F with respect to the order parameter C:

$$\phi = \frac{\delta F}{\delta C} = \frac{\lambda}{\epsilon^2}C(C^2-1) - \lambda\nabla^2 C \tag{2.12}$$

By minimizing F by C, which means, solve the equation $\phi(C) = 0$ with condition $C_{\mathrm{L}} = 1$ and $C_{\mathrm{G}} = -1$, equilibrium state in the interface can be described in one dimension:

$$C_e = \tanh\left(\frac{x}{\sqrt{2}\epsilon}\right) \tag{2.13}$$

the coordination x indicates the direction of the interface thickness. The interface thickness L_{di} is defined as the distance from $C = -0.9$ to $C = 0.9$, so that $L_{\mathrm{di}} = 2\sqrt{2}\epsilon \tanh^{-1}(0.9) \approx 4.16\epsilon$; the interface thickness within L_{di} contains 98.5% of the surface tension stress [18]. Since this interface with physical meaning is the key parameter to calculate the behavior of interface, it is always necessary to choose appropriate value and adequate mesh resolution for the interface for reliable simulations.

The interfacial tension can be expressed as the integral of the free energy density across the interface in equilibrium state [5]:

$$\sigma = \frac{2\sqrt{2}}{3}\frac{\lambda}{\epsilon} \tag{2.14}$$

Cahn and Hilliard [7, 6] extended the equilibrium equation to transfer equation for transient problems under assumption of proportional diffusive flux to chemical potential gradient:

$$\frac{\partial C}{\partial t} + (\mathbf{u} \cdot \nabla) = \kappa \nabla^2 \phi \tag{2.15}$$

where t, $\mathbf{u}$ and κ denote time, velocity and the CH mobility respectively. The term on the right side of equation 2.15 represent the diffusive process by the motion of the contact line on no-slip boundary conditions. A properly chosen κ is necessary to perform a accurate simulation of the motion of contact line. The wetting boundary condition for C is derived under assumption of wall free energy at local equilibrium:

$$\hat{\mathbf{n}}_s \cdot \nabla C = \frac{\sqrt{2}}{2}\frac{\cos(\theta)}{\epsilon}(1 - C^2) \tag{2.16}$$

where $\hat{\mathbf{n}}_s$ is the out pointing unit vector that is normal to the surface and ϵ is capillary width. Since this study concerns with two-phase flows of immiscible, incompressible, isothermal and Newtonian fluids, Navier-Stokes equation coupled with Cahn-Hilliard equation is applied as the governing equation:

$$\nabla \cdot \mathbf{u} = 0 \tag{2.17}$$

$$\frac{\partial}{\partial t}(\rho_c \mathbf{u}) + \nabla(\rho_c \mathbf{u} \otimes \mathbf{u}) = -\nabla p + \nabla \cdot [\mu_c(\nabla \mathbf{u} + \nabla \mathbf{u}^T)] + \mathbf{f}_\sigma + \rho_c \mathbf{g} \tag{2.18}$$

where p, $\mathbf{g}$ and $\mathbf{f}_\sigma$ denote the pressure, gravitational acceleration and inferfacial force. The interfacial force is defined as:

$$\mathbf{f}_\sigma = -C\nabla\phi \tag{2.19}$$

The subscript of density and viscosity in equation (2.18) denote that the density and viscosity of are calculated by order parameter C:

$$\rho_c = \frac{1+C}{2}\rho_{\mathrm{L}} + \frac{1-C}{2}\rho_{\mathrm{G}} \tag{2.20}$$

$$\mu_{\mathrm{c}} = \frac{1+C}{2}\mu_{\mathrm{L}} + \frac{1-C}{2}\mu_{\mathrm{G}} \tag{2.21}$$

where subscript L and G indicate the liquid phase and gas phase.

2.2.2 Discussion of Phase-Field Parameters

The characteristic length L is the diameter of the bubble for bubble rising study or the thickness of film between the cylinder and the bubble for the bubble cutting investigation. Both of the length are on the scale of millimeter or 0.1 millimeter whereas the physical thickness of interface is on the scale of 10 nanometers. Simulation covering these two scales is limited by the calculation expense. However, a properly selected and much thicker interfacial thickness will not impose influence on the result of simulation since only some global features of the bubble are of interest in this study. The dimensionless interface thickness Cahn number $Cn = \epsilon/L$ is introduced. The selection of Cn is based on the consideration of accuracy, stability efficiency [37]. The selection of Cahn number will be presented in the following chapters.

The accuracy of the simulation is affected by the mesh resolution, which is represented by mesh spacing h. Dimensionless mesh resolution within the diffusive interface N_{di} is introduced and will be discussed under different set-up and of different interest. N_{di} is the number of cells within the diffusive interface.

$$N_{\mathrm{di}} = \frac{L_{\mathrm{di}}}{h} \tag{2.22}$$

Another important parameter inherent to phase-field-method is the mobility factor κ. It quantifies the diffusive process of the motion of the contact line [39]. Since much larger interface thickness is applied in the simulation, it is hard to derive the mobility factor from theoretical calculation. Jacqmin [18] showed, $\kappa \propto O(\epsilon^2)$ ensures that the CH diffusion approaches zero as ϵ goes to zero, that is, conventional sharp-interface model could be properly recovered. Our value-fixing procedure for the phenomenological κ starts with a preliminary estimate following the relation:

$$\kappa = \chi\epsilon^2 \tag{2.23}$$

where χ serves as a pre-factor and can be slightly modified by validation with experiment results. Following the conclusion of Yue et al. [42], the mobility should be specifically determined by comparison with experiment data or theoretical calculation, since it may be considered as property dependent on certain physical feature system, where the material properties are of great significance.

2.2.3 Numerical Methodology

The implementation of phase-field method in this master thesis is based on the platform OpenFOAM®, (for "Open Source Field Operation And Manipulation") It is an open-source C++ toolbox for solving continuum mechanics problems, and therefore applied here to solve the computational fluid dynamics problem.

The solver *PhaseFieldFoam* is developed by Marshall and Cai. It is equipped with two options for solution procedure of the Cahn-Hilliard (CH) equation: segregated and coupled. Segregated scenario is applied in the calculation of this thesis, in which the solution procedure from time-step n to $n+1$ can be described as follows:

1. Calculate the chemical potential $\phi(t_n)$ using $C(t_n)$ with equation (2.12).
2. Update order parameter $C(t_{n+1})$ by solving equation (2.15) using $\phi(t_n)$ and $\mathbf{u}(t_n)$
3. Renew mixture density by equation (2.20) and mixture viscosity by equation (2.21) and new chemical potential by equation (2.12) and then interfacial tension $\mathrm{f}_\sigma(t_{n+1})$ by equation (2.19)
4. Finally solve the Navier-Stokes equations(2.17) , (2.18) to obtain velocity field.

This solution procedure works with initial and boundary condition so that the system of CH and NS equations can be solved.

2.2.4 Adaptive Mesh Refinement Method

Adaptive mesh refinement (AMR) can save considerable calculating resources considering the fact that the interface is moving and deforming during the process of cutting. Theodorakakos et al. [36] gave a general description of the development and process of adaptive refinement. Nikolopoulos et al. [26] made a VOF simulation for droplet impact on solid surface. The result shows good accordance with the result of an equidistant Cartesian mesh and the simulation shows better efficiency. Yu et al. [41] provided an example of 3D AMR in the investigation of deformation of a rising bubble (shown in figure 2.9). AMR are also applied in investigations based on phase field method. Chen et al. [10] developed a two dimensional, fully discretized and fully adaptive numerical scheme for physical model where Cahn-Hilliard equation and Navier-Stokes equations are coupled.

It should be noticed that AMR applied on bubble problems needs extra modification. The reason is tht the behavior of the bubble is also strongly dependent on the surrounding flow filed, which posses much larger inertia than that of interface and the gas phase in the bubble. As figure 2.9 shows, prediction of the bubble requires refinement for the bulk fluids.

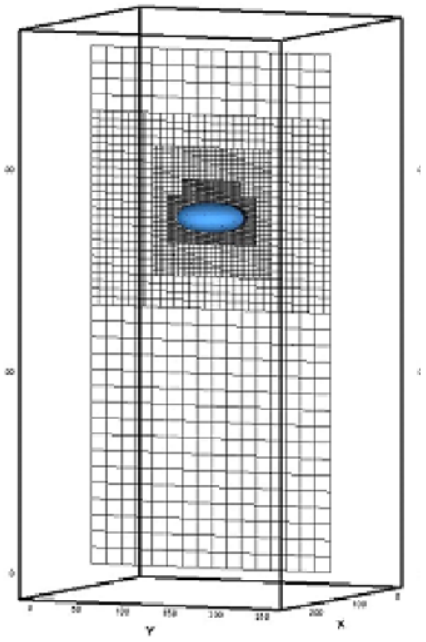

Figure 2.9: Adaptive mesh refinement for 3D bubble rising from Yu et al. [41]

The AMR method is supported by *phaseFieldFoam* 4.0. This refinement is controlled by several parameters. Comprehensive discussion and specific discretization strategy will be presented in Chapter 4.

3. Validation by Benchmark on 2D Bubble Rise

In this chapter, result of simulation from literature is selected for the validation of basic numerical parameter of phase field method. Identical set up and consistent physical parameters are applied in a simulation using *PhaseFieldFoam*. The set-up is introduced firstly and then the results of *PhaseFieldFoam* are given to validate the numerical method.

3.1 Setup of Benchmark

The benchmark chosen was conducted by Hysing et al. [32] under assumption of isothermal, incompressible flows of immiscible fluids. Dimensionless description is applied in the set up and the result. As shown in figure 3.1, the whole domain of size $[1 \times 2]$ is divided into two subdomains. Subdomain Ω_1 is occupied by fluid with larger density. The bubble domain of radius $r_0 = 0.25$ centered at $[0.5, 0.5]$. Domain Ω_2 contains the 'gas' fluid, whose density is much smaller than surroundings. The no-slip boundary condition is imposed to the top and the bottom. For the left and right boundaries, free-slip boundary conditions are applied.

The physical parameters are given in dimensionless form in the literature with characteristic length $L = 2r_0$ and time L/U_g, where $U_g = \sqrt{g2r_0}$. However, parameter with units must be provided for calculation of *PhaseFieldFoam*. Hysing et al. [32] characterized this case by Reynolds number Re and Bond number Bo, which are defined as

$$Re = \frac{\rho_1 U_g L}{\mu_1} \tag{3.1}$$

$$Bo = \frac{\rho_1 U_g^2 L}{\sigma} \tag{3.2}$$

Density ratio and the viscosity ratio, ρ_1/ρ_2 and μ_1/μ_2 of the "liquid" and "gas" serve to determine the physical properties of the two fluids and therefore should be the same as in the benchmark. Typical characteristic length, time and mass of bubble rising problems in reality are selected for *phaseFieldFoam* and the other parameters are calculated based on the similarity mentioned above. The transfer result is shown in figure 3.1.

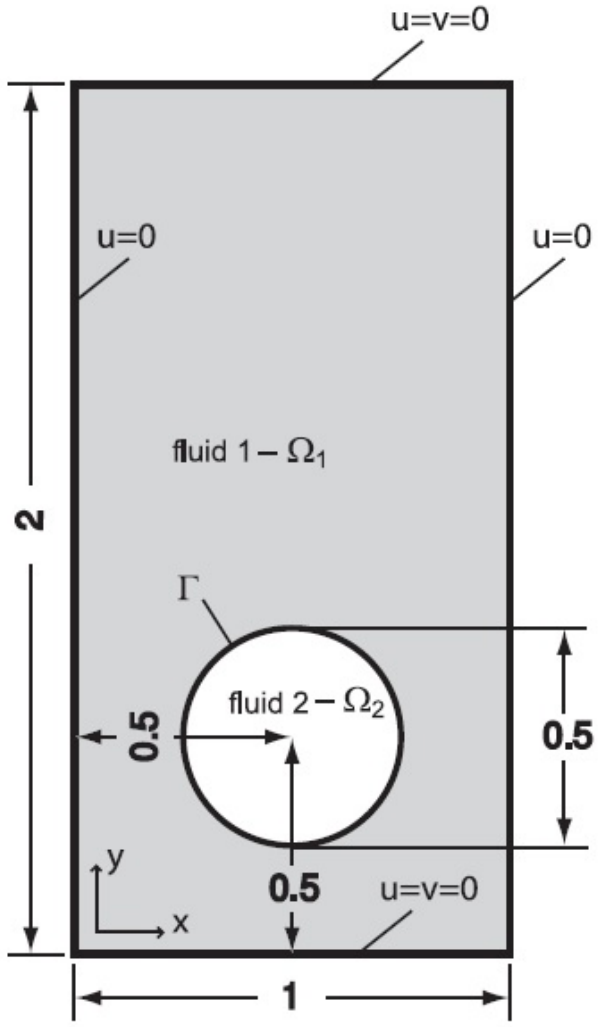

Figure 3.1: Initial configuration and boundary conditions for benchmark case [32].

Table 3.1: Transfer of dimensionless parameters in benchmark by Hysing et al. [32] into parameters applied in *phaseFieldFoam* calculation.

	Dimensionless	Scaled valued with unit
L	1	10 mm
ρ_1	1000	1000 kg/m^3
ρ_2	100	100 kg/m^3
μ_1	10	0.0136 kg/(m · s)
μ_2	1	0.001 36 kg/(m · s)
g	0.98	9.8 m/s^2
σ	24.5	0.0245 N/m
Re	35	35
Eo	10	10
ρ_1/ρ_2	10	10
μ_1/μ_2	10	10

The boundary condition of the setup in the validation is identical as in the literature [32]. Initial condition of *phaseFieldFoam* is given in figure 3.2. Diffusion region instead of sharp interface are applied on the boundary of the bubble, since diffusive interface is the main

feature of phase field method. Thickness of interface is characterized by Cahn number. In this validation, calculations with $Cn = 0.01$ and $Cn = 0.02$ are performed to investigated the influence of interface thickness. This range of Cahn number is applied by Hosseini et al. [31] and shows good match with the reference. Uniform mesh is applied with a reasonable resolution with N_{di}=4 and N_{di}=8. Definition of N_{di} is given in equation (2.22). The interface and the resolution of the mesh varies from [200× 400] to [400× 800] and the cell size h varies then from $h = 0.05\,\mathrm{mm}$ and $h = 0.025\,\mathrm{mm}$ accordingly. A variety of dimensionless mobility prefactor χ from $4\,\mathrm{kg}\cdot\mathrm{m}\cdot\mathrm{s}^{-1}$ to $10\,\mathrm{kg}\cdot\mathrm{m}\cdot\mathrm{s}^{-1}$ is investigated in this validation. Constant time step of typically $\Delta t = 10^{-6}\,\mathrm{s}$ is applied ensure numerical stability of the calculation.

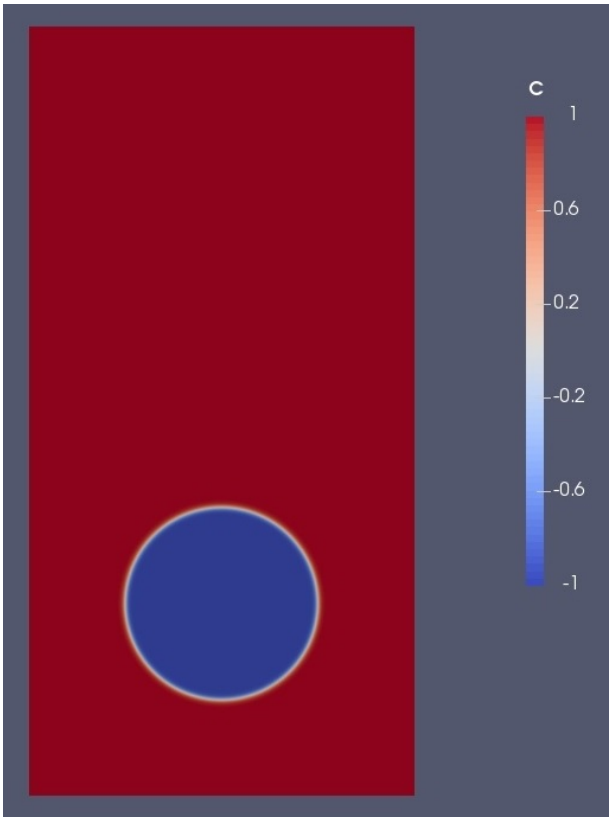

Figure 3.2: Initial configuration for benchmark case

3.2 Validation Results

Comparison between the results and benchmark is performed both qualitatively and quantitatively. The velocity U_b^* evolution of bubbles in the reference and velocity that is obtained in *PhaseFieldFoam* are given here besides the visual comparison of bubble shape at different time points. Bubble velocity is defined by equation (3.3)

$$U_b = \frac{\int_{\Omega_2} u \mathrm{d}x}{\int_{\Omega_2} 1 \mathrm{d}x} \tag{3.3}$$

and the U_b is transferred into dimensionless form U_b^* by equation (3.4)

$$U_b^* = \frac{U_b}{U_g} \tag{3.4}$$

where U_g is obtained from the physical properties applied in *phaseFieldFoam* calculation. Dimensionless time t^* is defined by equation (3.5)

$$t^* = \frac{t \cdot U_g}{L} \tag{3.5}$$

Figure 3.3 presents the comparison between result of *PhaseFieldFoam* test case under different configurations and reference data. It can be observed that bubble undergoes a acceleration process at the beginning driven by the buoyancy. Peak value of velocity arises around dimensionless time $t^* = 0.9$. The bubble decelerates then until a constant velocity is obtained from $t^* = 2.5$. The results of *PhaseFieldFoam* share the same feature of the reference data generally and difference due to numerical parameters can also be observed. The velocity evolution obtained with $N_{\mathrm{di}} = 8$ is consistent with the reference perfectly whereas curves obtained by $N_{\mathrm{di}} = 4$ shows small deviation.

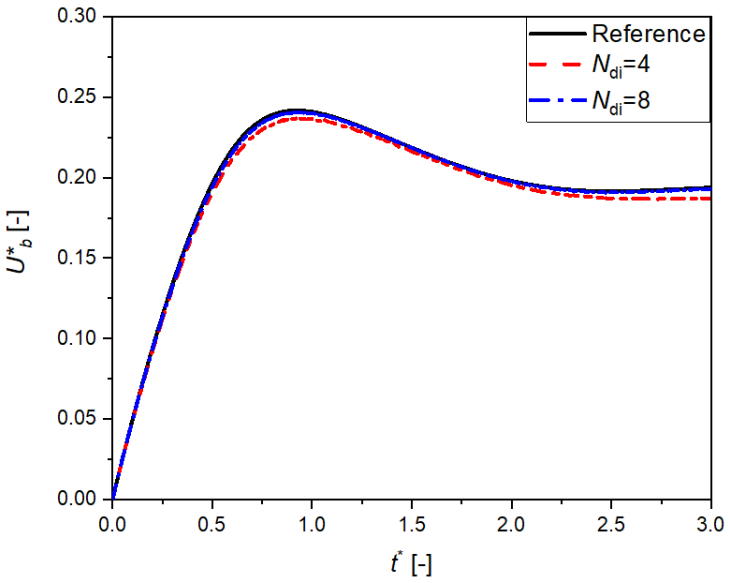

Figure 3.3: Influence of mesh resolution, $Cn = 0.01$, χ=8 kg · m · s^{-1}

The first significant difference arises near the peak. Peak value of $N_{\mathrm{di}} = 4$ is smaller than the reference and the peak velocity is also later attained. A more important difference is the end state where the case $N_{\mathrm{di}} = 4$ obtains a smaller end velocity and the deceleration process is also longer than the reference and the set-up with better mesh quality. Since the interface and the bulk fluid share the same resolution in uniformly discretized domain, there is two possible reasoning. The first possibility lies in the failure of a correct physical description of the interface and with equal likelihood, of the bulk fluid near the interface. This surrounding fluids is of essential importance to the drag force of the bubble.

Figure 3.4 shows the influence of Cahn number on rising velocity. Both of the *PhaseFieldFoam* results show good match with the reference data. There is only slightly larger difference with the reference data of peak velocity and end velocity value of the case $Cn = 0.02$ than the case $Cn = 0.01$. Since then it can be concluded that currently used Cahn numbers have successfully reached the sharp-interface assumption.

Figure 3.5 shows the comparison of results under different mobility parameters in the form of pre-factor χ defined in equation (2.23). It can be seen that larger mobility leads to higher rising velocity of the bubble. The curves match well with the reference data when $\chi = 8\,\mathrm{kg} \cdot \mathrm{m} \cdot \mathrm{s}^{-1}$ and $\chi = 10\,\mathrm{kg} \cdot \mathrm{m} \cdot \mathrm{s}^{-1}$. For $\chi = 4\,\mathrm{kg} \cdot \mathrm{m} \cdot \mathrm{s}^{-1}$, however, there is relatively larger difference. The most significant difference at the terminal state where the velocity of case $\chi = 4\,\mathrm{kg} \cdot \mathrm{m} \cdot \mathrm{s}^{-}1$ is much smaller than the other curves. An explanation of this remarkable difference would be, the combination of thickness of diffusion area and

mobility does not provide precise modeling to approach sharp edge assumption.

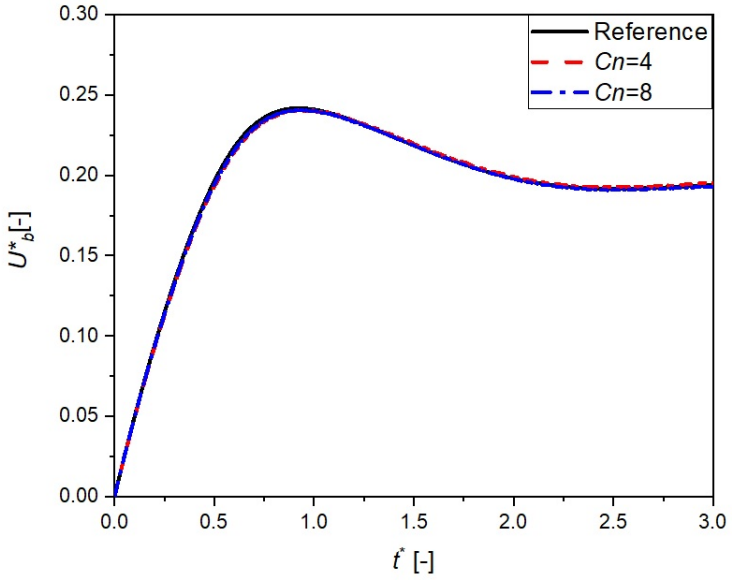

Figure 3.4: Influence of Cahn number, N_{di}=8 , χ=8 $\mathrm{kg \cdot m \cdot s^{-1}}$.

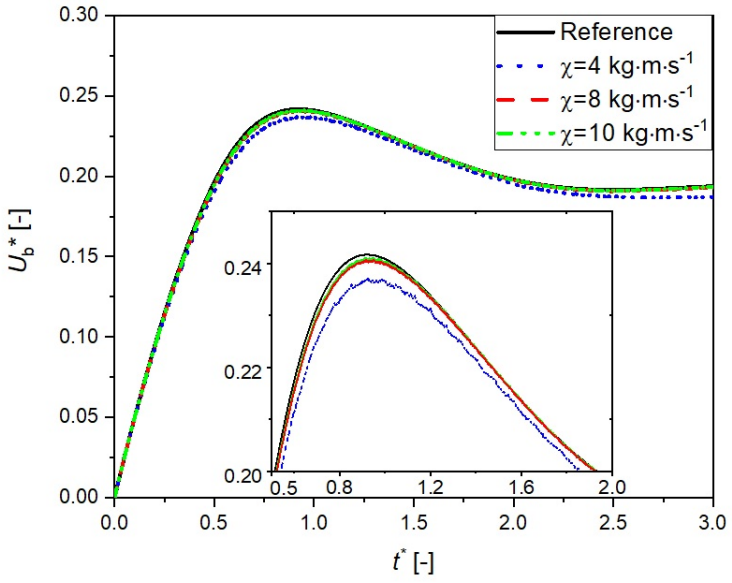

Figure 3.5: Influence of mobility, Cn=0.01, N_{di}=8.

In addition to the terminal velocity, the inset figure in figure 3.5 shows the detail near the peak of the curve. Difference at the peak value can also be observed with different mobility.

Figure 3.6 compares the bubble shape at dimensionless time $t^* = 3$. The bubble shape under $Cn = 0.01$, $N_{\mathrm{di}} = 8$, and $\chi = 8\,\mathrm{kg \cdot m \cdot s^{-1}}$ is shown since it shows a reasonable match in velocity profile with the reference. The red curve is the result of *PhaseFieldFoam* and the black curve is the reference. It can be observed that the bubble shape calculated

by *PhaseFieldFoam* shows a overall identical shape. The very small non-overlapping region shows that the length to height ration of the bubble generated by *PhaseFieldFoam* is slightly smaller than the reference data.

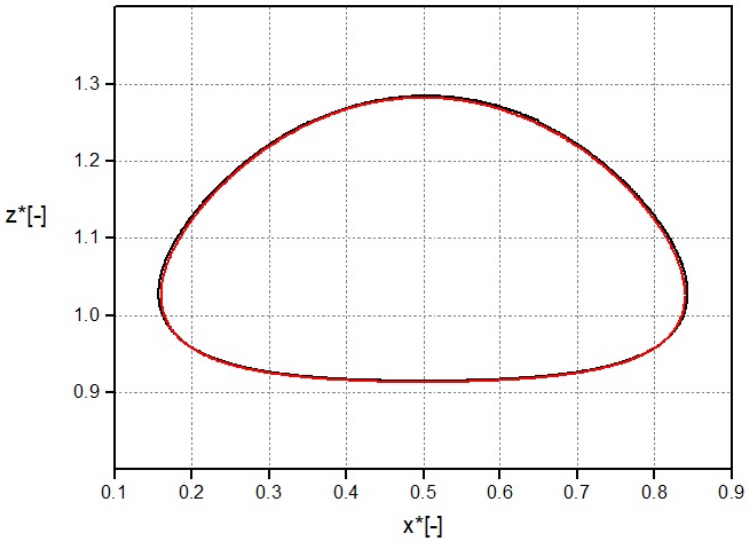

Figure 3.6: Bubble shape comparison of benchmark, black curve is the reference data, red curve is the result of *PhaseFieldFoam*

In this section, *phaseFieldfoam* is validated with benchmark from literature. Different numerical parameters are investigated and the parameter combination $Cn = 0.01, N_{\mathrm{di}} = 8$, $\chi = 8\,\mathrm{kg} \cdot \mathrm{m} \cdot \mathrm{s}^{-1}$ shows the best match on both velocity profile and interface behavior and consumes reasonable calculation resources.

4. Simulation on Bubble Cut and Comparison with Experiment

In this chapter, results of simulations with different bubble size are presented. The bubble size and the cutting geometry are selected in reference of experiment composed by Rohlfs [30]. Simulation without solid cylinder is made at first for optimization of the numerical parameters and simulation domains. Preliminary investigation of bubble cutting is performed in planar domain. Finally, 3D simulation results of bubble cutting provides comprehensive understanding of the cutting phenomena and allows a comparison with experiment results.

4.1 Simulation of Free Bubble Rising with Axisymmetric Set Up

This section shows simulation results of bubble rising. Two equivalent diameters (defined by equation (2.1)) of the bubble are investigated with axisymmetric set-up to reduce the calculation expense. These simulations are composed to determine the necessary length of the domain, which is relevant to the rising distance from initial state to the constant state of the bubble. Minimization of this length is essential to reduce the cell number and physical time of the simulation, which is of importance for the 3D simulation. The constant rising velocity and aspect ratio are then compared with correlation from literature [1, 28] to validate the numerical parameter of phase field method.

4.1.1 Simulation Set Up

Glycerin-water mixture with weight percent 90% is used in Rohlfs' [30] experiment. All the properties of the mixture are calculated from literature [11, 35] under temperature of 20 °C. The physical properties are given in table 4.1

Table 4.1: Physical properties in the simulation

ρ_L	ρ_G	μ_L	μ_G	g	σ
$1237.42\,\mathrm{kg/m^3}$	$1.204\,\mathrm{kg/m^3}$	$0.219\,\mathrm{kg/(m\cdot s)}$	$0.000\,018\,\mathrm{kg/(m\cdot s)}$	$9.8\,\mathrm{m/s^2}$	$0.066\,\mathrm{N/m}$

The numerical configurations are firstly validated by the terminal velocity of the rising bubble and then, terminal aspect ration is further compared by correlation introduced in

equation (2.8) from Aoyama et al. [1]. The reference terminal velocity is calculated in equation (4.1) by Park et al. [28]

$$U_{\mathrm{b,terminal}} = \frac{1}{\sqrt{f_{sc}^2 \cdot \left(\frac{144 \cdot \mu_L^2}{g^2 \cdot \rho_L^2 \cdot d_{\mathrm{eq}}^4} + \frac{\mu_L^{4/3}}{0.14425^2 \cdot g^{5/3} \cdot \rho_L^{4/3}}\right) + \frac{1}{\frac{2.14\sigma_L}{\rho_L \cdot d_{\mathrm{eq}}} + 0.505 \cdot g \cdot d_{\mathrm{eq}}}}} \tag{4.1}$$

where

$$f_{sc} = 1 + \frac{0.5}{1 + \exp(\frac{\log Eo + 1}{0.38})}$$

Bubbles with two different diameters are investigated in this section. The corresponding characteristic numbers and reference terminal state of investigated bubbles are shown in figure 4.2.

Table 4.2: Characteristic number of bubble rising and cutting

d_{eq}	V_{B}	Re	Eo	$U_{\mathrm{b,ref}}$	$A_{\mathrm{r,ref}}$
7.8 mm	250 ml	6.00	9.73	136.2 mm/s	0.71
9.85 mm	500 ml	11.17	17.81	174.8 mm/s	0.54

The bubble rising phenomena is axisymmetric so that corresponding set-up can be applied and hence greatly reduce the calculation expense.

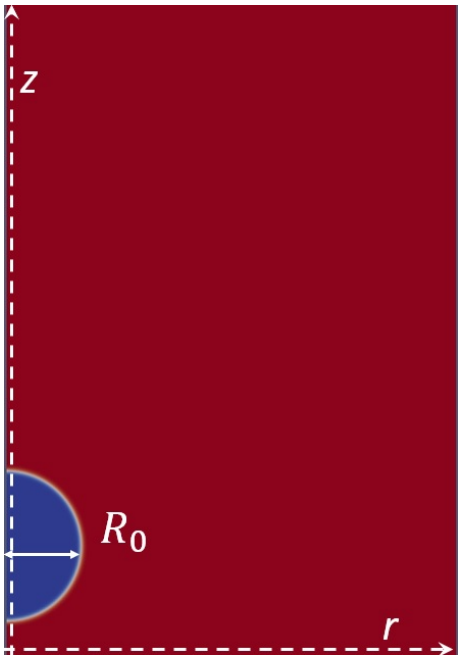

Figure 4.1: Smoothing of initial order parameter field

Figure 4.1 shows the initial distribution of order parameter. The bubble starts from perfect spherical shape with $R_0 = \frac{1}{2} d_{\mathrm{eq}}$. The fluid field is set to be at rest initially. As Cai et al. [8] suggested, the total width of the domain W is set initially $W = 5 d_{\mathrm{eq}}$, a large total domain height $H = 9 d_{\mathrm{eq}}$ guarantees that there is enough space for the full development of the bubble. This domain is discretized by stationary structured and homogeneous grids. Previous investigation [8] shows that a precise prediction of the cutting behavior requires a smaller Cahn number than $Cn = 0.02$. Considering this conclusion and limited by the calculation ability, simulations with a reasonable Cahn number $Cn = 0.01$ are applied in this chapter. The resolution of the domain is [300×900], which means $N_{\mathrm{di}} = 4$ and there

is 100 cells in the the length of diameter of the bubble.

Free slip boundary condition are applied at $r = W$. For the top and bottom, boundary condition $pressureInletOutletVelocity$ for velocity and fixed 0 relative pressure are used. The order parameter C for Cahn-Hilliard equation are set to be zero gradient for all the boundaries that are included in the axisymmetric calculation.

4.1.2 Results of Free Bubble Rise

Since the interface thickness and the mesh resolution is already given in the previous section, the last numerical parameter mobility is discussed here. The pre-factor of mobility defined in equation (2.23) is chosen as the symbol of mobility discussed in the following sections.

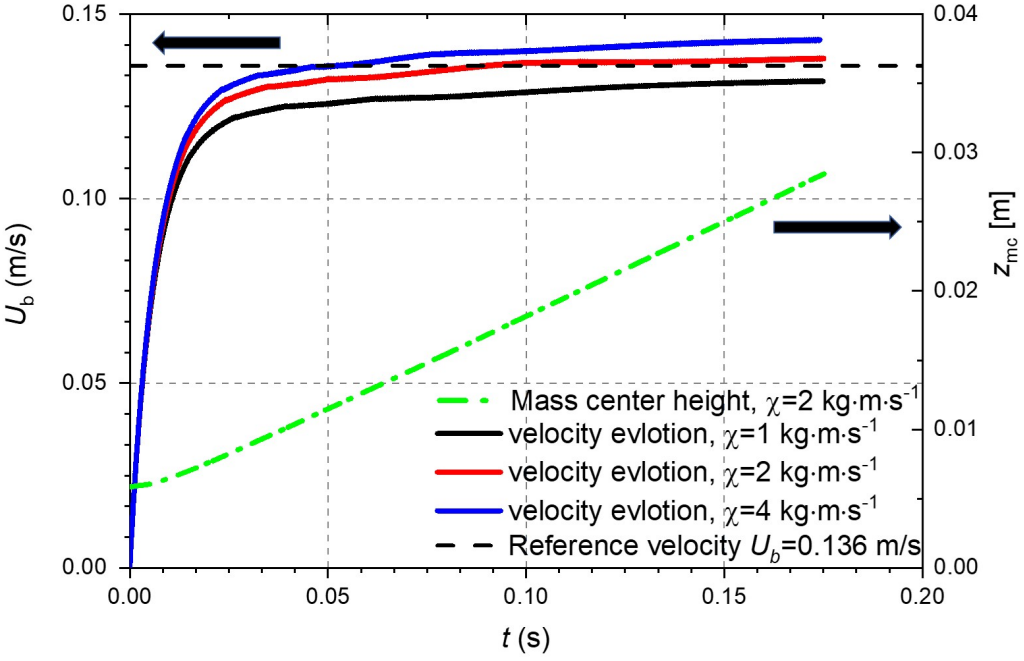

Figure 4.2: Influence of mobility on rising velocity of bubble with $d_{\mathrm{eq}} = 7.8\,\mathrm{mm}$, $Cn = 0.01$, $N_{\mathrm{di}} = 4$.

Figure 4.2 and 4.3 compare the rising velocity evolution of the bubble with $d_{\mathrm{eq}} = 7.8\,\mathrm{mm}$ and $d_{\mathrm{eq}} = 9.85\,\mathrm{mm}$, respectively. Note that the mass center position history of $d_{\mathrm{eq}} = 7.8\,\mathrm{mm}$ is provided here for AMR validation in section 4.3. It can be observed that all velocity evolution of the same bubble diameter share the same feature: the smaller bubble with $d_{\mathrm{eq}} = 7.8\,\mathrm{mm}$ keep accelerating until constant velocity is reached; the rising velocity of the larger bubble with $d_{\mathrm{eq}} = 9.85\,\mathrm{mm}$, due to oscillation caused by stronger deformation, undergoes a deceleration process before the terminal velocity after a small peak. Influence of different mobility can be also observed on the terminal rising velocities, which show notable variation. Larger mobility again increases the terminal velocity, which is firstly observed in the validation stage. Since this influence of mobility, which is only investigated for wetting phenomena with moving contact line [43], is still not quantitatively investigated for bubble rising case, selection of mobility must be based on comparison between the terminal velocity obtained in simulation and experimental/ analytical results. According to

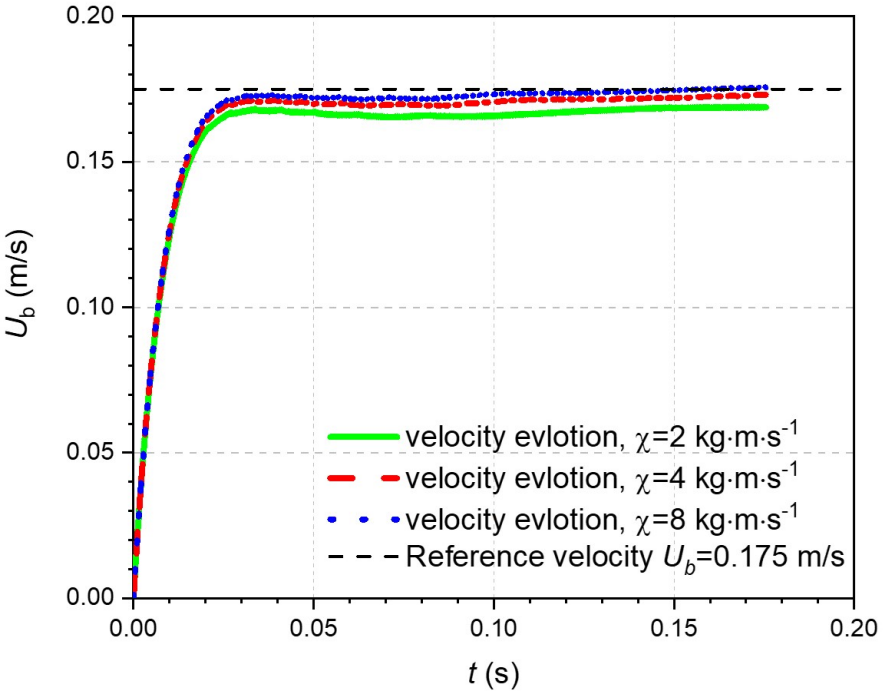

Figure 4.3: Influence of mobility on rising velocity of bubble with $d_{\mathrm{eq}} = 9.85\,\mathrm{mm}$, $Cn = 0.01$, $N_{\mathrm{di}} = 4$.

the comparison, $\chi = 2\,\mathrm{kg \cdot m \cdot s^{-1}}$ as the mobility pre-factor for $d_{\mathrm{eq}} = 7.8\,\mathrm{mm}$ and for bubble with $d_{\mathrm{eq}} = 9.85\,\mathrm{mm}$, the mobility pre-factor is chosen as $\chi = 8\,\mathrm{kg \cdot m \cdot s^{-1}}$.

The duration and distance of rising until the terminal state are also of interest, since the terminal state must be reached before cut by solid cylinder in the following simulations. For both cases there is no notable change of velocity after $t = 0.1\,\mathrm{s}$. It is assumed that the bubble undergoes no velocity change and deformation process after this time point here.

Figure 4.4 and 4.5 show the terminal shapes of the bubbles with $d_{\mathrm{eq}} = 7.8\,\mathrm{mm}$ and $d_{\mathrm{eq}} = 9.85\,\mathrm{mm}$, respectively for further confirmation of the terminal state. The aspect ratio A_r by equation (2.7) is used here to compare the bubble shape quantitatively. The width w and height h of the deformed bubble in simulation result are calculated by equation (4.2) and equation (4.3)

$$w = 2 \cdot \max r_{\mathrm{n}} \tag{4.2}$$

$$h = \max z_{\mathrm{n}} - \min z_{\mathrm{n}} \tag{4.3}$$

where subscript n denotes the points on the "neutral" surface where $C = 0$ is valid. Both aspect ratios calculated by *PhaseFieldFoam* are slightly larger than the correlation (given in table 4.2). A possible reason is that the shape development is slower than the velocity development and it requires much longer time and distance to reach the very precise terminal shape as the correlation indicates. Considering the fact that the bubble will undergo intensive deceleration and shape changing process before reaching the cylinder, the influence of this small deviation is assumed to be acceptable.

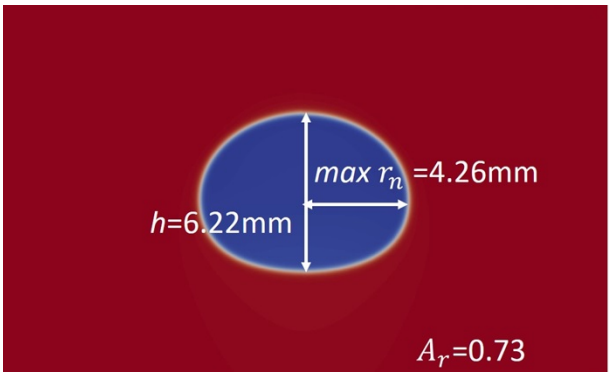

Figure 4.4: Bubble shape of $d_{\text{eq}} = 7.8\,\text{mm}$ at t=0.1 s

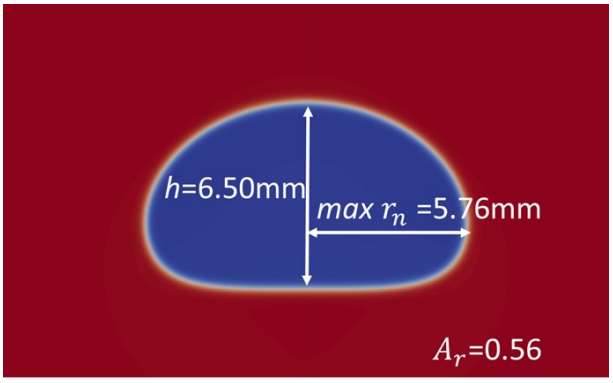

Figure 4.5: Bubble shape of $d_{\text{eq}} = 9.85\,\text{mm}$ at t=0.1 s

4.2 2D Simulation of Bubble Cutting in a planar domain

2D simulation for bubble cutting is performed in a planar domain as preliminary investigation for the cutting behavior. This simulation fails to provide very accurate physical description of the rising as well as cutting of the bubble since law of mass conservation keeps the constant area of the 2D bubble whereas it is the volume of the bubble that keeps constant in the reality and the cross-sectional area does not necessarily keeps the same. This simulation, however, is able to provide the most of the characteristic and qualitative description on the cut with reasonable calculation expense and duration. Another advantage is, comparison between 2D and 3D simulation helps for understanding of the 3D evolution of bubble shape by the interaction with a solid cylinder.

Two possibility of interaction of bubble-cylinder interaction, namely, the cutting and slip-off are investigated in planar domain in this section. Two different bubble diameter are investigated according to the experiment [30], which show different hydrodynamic interaction behaviors.

4.2.1 Set Up of Planar Domain for the 2D Simulation

The selection of the bubble size is based on the experiment of Rohlfs [30]. Since then all physical properties and the numerical set-up characterized by Cn, N_{di} and χ identical with the fee rising simulation.

The cutting phenomena that happens on larger bubble is assumed here perfectly symmetric and only half of geometry is included in the simulation. The boundary condition and initial order parameter for bubble with $d_{\text{eq}} = 7.8\,\text{mm}$ are given in figure 4.6. Shown in figure 4.6, the gas phase is half-spherical shaped at rest. The solid cylinder with diameter

$d = 4\,\text{mm}$ in the middle of the domain is impermeable and no-slip wall for velocity with a constant contact angle for order parameter C. Influence of wettability are investigated by different boundary condition on the cylinder. In this thesis, contact angle $\theta = 60°$, $\theta = 90°$ and $\theta = 120°$ which represent typical hydrophobic, neutral and hydrophobia surface are investigated. The mathematical description of this boundary is given in equation (2.16). Boundary condition *fixedFluxPressure* is applied for the solid cylinder for pressure. The left boundary is set to be symmetric boundary to reduce the calculation cost. All the lateral boundaries that are normal to the third direction is set to be *empty* so that the governing equations are solved in two-dimension. The other boundary condition, namely the top, the bottom and the lateral boundary on the right is the same in the axisymmetric simulation shown in table 4.1.

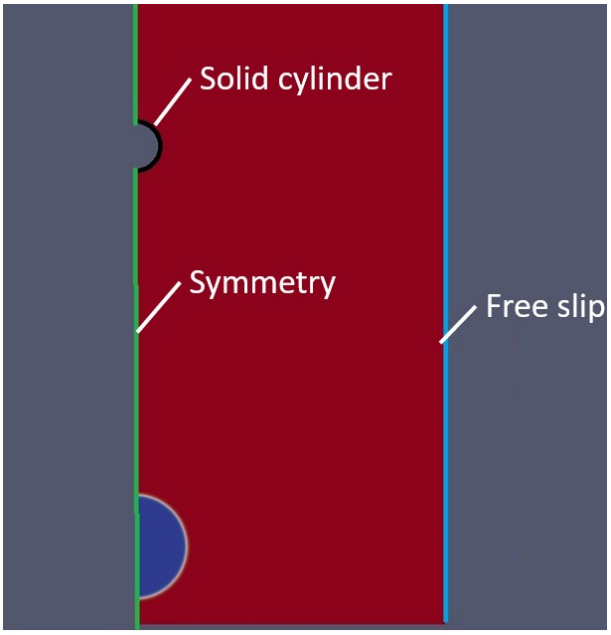

Figure 4.6: Initial and boundary condition for planar cut $d_{\text{eq}} = 7.8\,\text{mm}$

Verified in the previous simulation, the width of the domain is $W = 2.5d_{\text{eq}}$ and the height is $H = 8d_{\text{eq}}$. Uniform, homogeneous mesh with resolution [300×800] is applied to discretize the domain with cell size $h = 7.8 \times 10^{-2}\,\text{mm}$.

Interaction of a rising bubble and a solid cylinder can lead to different outcome. Besides the cutting phenomena which is the main focus of the thesis, smaller bubble will slip over the cylinder under the stronger influence of surface tension, which keeps the bubble undivided. This phenomena is observed by in the experiment of Rohlfs [30] on a small bubble with $d_{\text{eq}} = 4.57\,\text{mm}$. Since smaller bubble undergoes relatively smaller deformation, simulation in a planar domain is expected to show better accordance with the experiment.

As shown in figure 4.7, the planar domain of the bubble-slip case shares the same solid cylinder with $D_{\text{cylinder}} = 4\,\text{mm}$ with previous set-up (shown in figure 4.6) on the center line of the domain. The center of the bubble is shifted from the center line with a small offset of 0.1 mm in positive x direction so that the bubble is expected to slip over the cylinder form the right side. The whole bubble and cylinder are included in the domain since symmetry is no longer valid in the initial condition. Total height of the domain is in this case $6d_{\text{eq}}$ and total width is $4d_{\text{eq}}$. The domain is descretized by uniform, homogeneous with resolution $[400 \times 600]$. The cell size is here correspondingly $h = 4.57 \times 10^{-2}\,\text{mm}$. Free slip boundary condition is imposed on the lateral boundaries. The other boundary conditions

are kept identical with the planar cutting set-up.

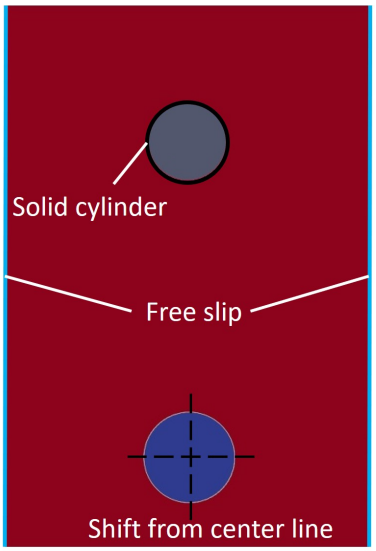

Figure 4.7: Initial and boundary condition for the case slip over $d_{\mathrm{eq}} = 4.57\,\mathrm{mm}$

4.2.2 Results and Discussion

The bubble shapes of experimental investigation [30] and simulation of *phaseFieldFoam* are shown in figure 4.8. A comparison between the experiment and planar numerical simulation with θ =60° is made at first, and then the influence of contact angle is discussed.

It can be seen that 2D simulation can already provide a close description of the shape as in the experiment: the gas phase concentratse to the left and right side of the bubble under influence of the solid cylinder, and the connection at the bottom of the cylinder gets thinner to the thread shape until the upper and lower gas-fluid interface contact with each other and two daughter bubbles are generated.

Deviation due to absence of consideration of the flow in the third direction can also be observed. The first difference lies in the lateral extension before the contact. The 2D extension is obviously stronger than what experiment shows due to absence of surface tension in the third direction. This over-extension also accelerates the whole cutting process and leads to a much thinner connection on the bottom of the cylinder, which is can be observed in figure 4.8e. Besides this difference, liquid film between the solid cylinder and bubble is thicker than the experiment result. This deviation is of importance since the existence of liquid film is relevant to the independence of interface behavior on wettability of the cylinder surface. The reason for this difference may be the flow of gas phase in the third direction and will be discussed in next section with more detail provided by 3D simulation. There is one more major difference at the end of the cutting process: the generation of satellite bubble in *phaseFieldFoam* simulation shown in figure 4.8f. This small bubble cannot be found in the photos of experiment as shown in figure 4.8c. Since the generation of satellite bubble is related to the break-up of liquid film, this difference may be also explained by the 3D flow of the cutting process. There is one more potential reason: the sharp interface may not be reached under the interface thickness since the thickness of liquid film or even smaller length may play a more important role during the break of the liquid film and they are much smaller than the bubble diameter cause much larger ”local” Cahn number at the bottom of the cylinder.

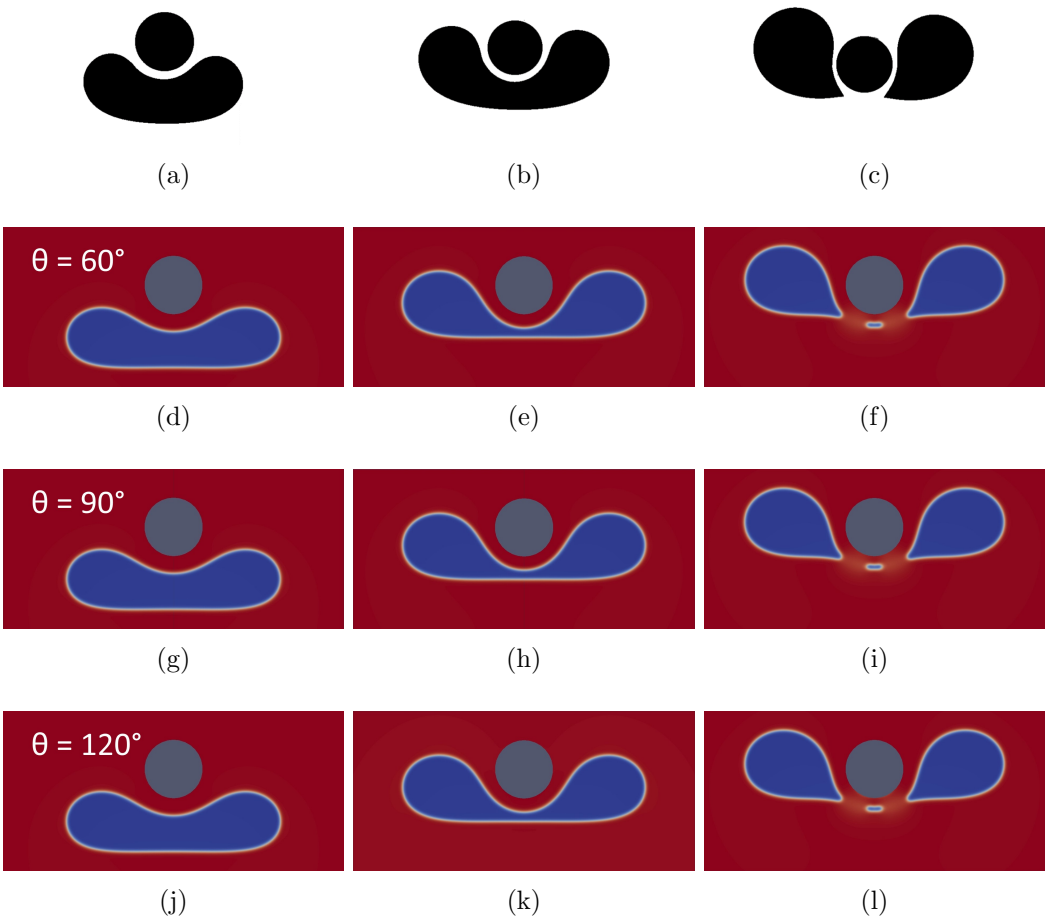

(a) (b) (c)

(d) (e) (f)

(g) (h) (i)

(j) (k) (l)

Figure 4.8: Comparison of bubble deformation of bubble cutting, $d_{eq} = 7.8\,mm$. (a)-(c): bubble shape evolution in experiment [30]. (d)-(f): profile of order parameter in planar simulation of *phaseFieldFoam*, $\theta = 60°$, (g)-(i): profile of order parameter in planar simulation of *phaseFieldFoam*, $\theta = 90°$, (j)-(l): profile of order parameter in planar simulation of *phaseFieldFoam*, $\theta = 120°$.

The influence of wettability is investigated by comparison of the bubble shape evolution by different contact angle. Instead of being partially wetted in previous simulation (figure 2.7), the cylinder surface are completely covered by liquid film and the behavior of the bubbles under different contact angle are identical, which is in accordance with the experiment result [30]. Since the liquid film avoids the direct contact between the bubble and cylinder and hence the generation of contact line where influence of contact angle is taken into consideration, wettability will not affect the behavior of the bubble if the cylinder is completely covered by the liquid film. However, simulation in planar domain is not able to provide very precise prediction of the thickness of the liquid film, and to prove that the existence of the liquid film. Quantitative, 3D simulation is performed to discuss the details of liquid film in the next section.

Figure 4.9 compares the bubble shape of in the slip-over case obtained in the experiment investigation [30] and the simulation in the planar domain. The bubble undergoes smaller deformation and bubble keeps a more spherical shape for the reason that surface tension is stronger than the buoyancy and viscous force in a smaller bubble. Since more gas phase is concentrated near the center of the bubble buoyancy on the left and right part that tends to drive the bubble apart in figure 4.8 is in this case over-weighted by the surface tension.

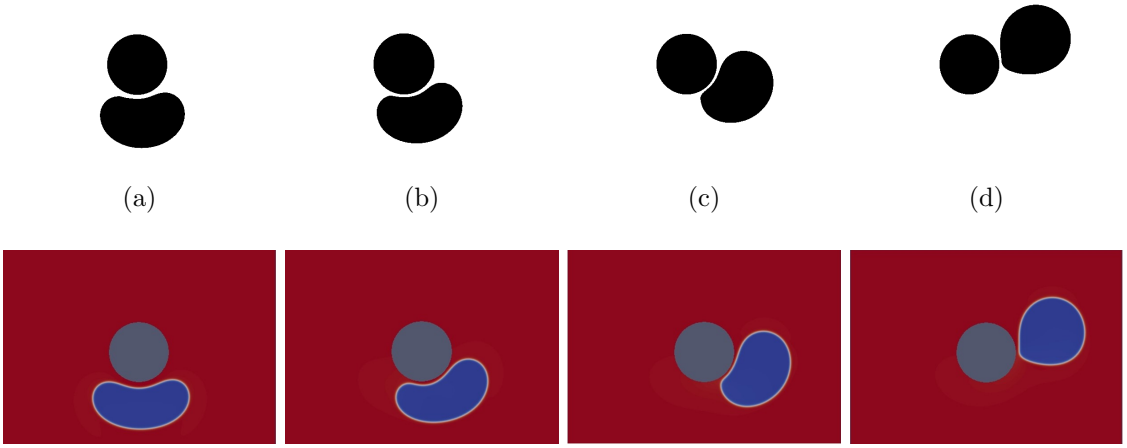

Figure 4.9: Comparison of bubble deformation of bubble slip-over, $d_{\text{eq}} = 4.57\,\text{mm}$. (a)-(d): bubble shape evolution in experiment [30]. (e)-(h): smoothing of order parameter ordained in planar simulation of *phaseFieldFoam*.

Shown in figure 4.9f, the left part of the bubble is dragged by the surface tension from the bottom to the right side and the bubble keeps intact during the whole interaction process. Despite the over-extension due to the the absence of surface tension in the third direction discussed in the previous simulation, the result obtained by *phaseFieldFoam* is in better accordance with the experiment result. The bubble shape in figure 4.9g and figure 4.9h is very similar to the bubble shape in the experiment. There are potentially two reason for improved similarity. The first reason lies in the overall smaller deformation inherent in smaller bubbles by free rising, which will reduce the deviation by defected planar set-up. The second reason is that the bubble keeps intact instead of being cut by the cylinder, which can not be predicted in a planar simulation precisely. Since simulation in a planar domain provides a satisfactory result bubble slip over, the 3D simulation will be focused on the bubble cutting phenomena, which finds also much more application.

4.3 3D Simulation of Bubble Cutting with Adaptive Refinement

This section shows the result of 3D simulation of bubble cutting investigated by previous section, with specific developed mesh refinement strategy. The descretization method is discussed at first and validated by the comparison to the simulation with uniform mesh. The bubble cut is shown and evaluated finally.

4.3.1 Simulation Set Up

The set-up of 3D simulation is based on the validation of the previous simulation. The physical properties and the characteristic numbers are shown in figure 4.1 and table 4.2. Since the domain is symmetric in two directions, 1/4 of the physical domain is included in this simulation, with "*Symmetry*" boundary condition on the front and left boundary of the domain. The total width and depth of the domain are $2.5d_{\text{eq}}$. The domain consists of two parts: the lower parts provide space for the free rising of the bubble, until the terminal velocity and shape are reached and after the terminal state is reached. The upper part provides the space for the flow field during and after the cut. Figure 4.2 shows the velocity and the height of the mass center of the bubble discussed in section 4.1. To determine the size of the domain, the distance of free rising is obtained from figure 4.2. In this case

the rising distance at $t = 0.1\,\mathrm{s}$ is used. Extra distance between this position and the solid cylinder center is also required to guarantee that this free rising is not affected by the cylinder before the terminal bubble velocity is reached.

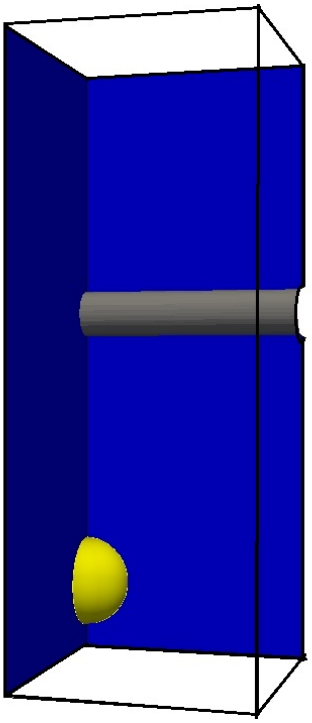

Figure 4.10: Initial condition of the 3D simulation

Figure 4.10 shows the initial condition of the 3D simulation. The yellow sphere denotes the interface where $C = 0$. The symmetric boundary is shown in blue and the other lateral boundary are set as *freeSlip*. The gray column indicates the solid cylinder and the boundary condition of the top, the bottom and the cylinder keep the same as in the previous simulations.

The domain was discretized by uniform mesh in the axisymmetric or 2D simulation. The same mesh set-up is, however, hard to realize in 3D simulation due to the increase of mesh size. The number of cells in a 2D simulation is, for instance, 3×10^5 whereas 3D domain under the same resolution requires approximately 8×10^7 cells. This extremely large number of cells is not only limited by calculation resources but also by efficiency of the parallel processing executed by multiple processors. Considering the fact that high resolution is only necessary within and near the interface which possesses small volume, whereas mesh with much coarse resolution can already meet the requirement of single phase flow in the rest of domain, local refinement is a reasonable way to reduce the calculation expense.

Since the interface is of most interest, the order parameter C is selected as "controller" of the adaptive refinement. Refinement on $-0.97 < C < 0.97$ shows good independence at the same time avoid unnecessary refinement to reduce the expense of calculation. The mesh is renewed in every 10 time steps. The displacement of the interface within the refinement interval Δs_{RI} is given in equation 4.4:

$$\Delta s_{\mathrm{RI}} = n_{\mathrm{RI}} \cdot \Delta t \cdot U_{\mathrm{b,terminal}} \tag{4.4}$$

where n_{RI} denotes the number of time step within a refinement interval. The time step Δt is $10^{-6}\,\mathrm{s}$ in this simulation. The terminal velocity is obtained in the free-rising case given in table 4.2. The displacement Δs_{RI} is then in the order of $10^{-6}\,\mathrm{m}$, whereas the length

of a cell in the interface is in the order of 10^{-5} m. Proved by the calculation above the solution process can be assumed numerically stable.

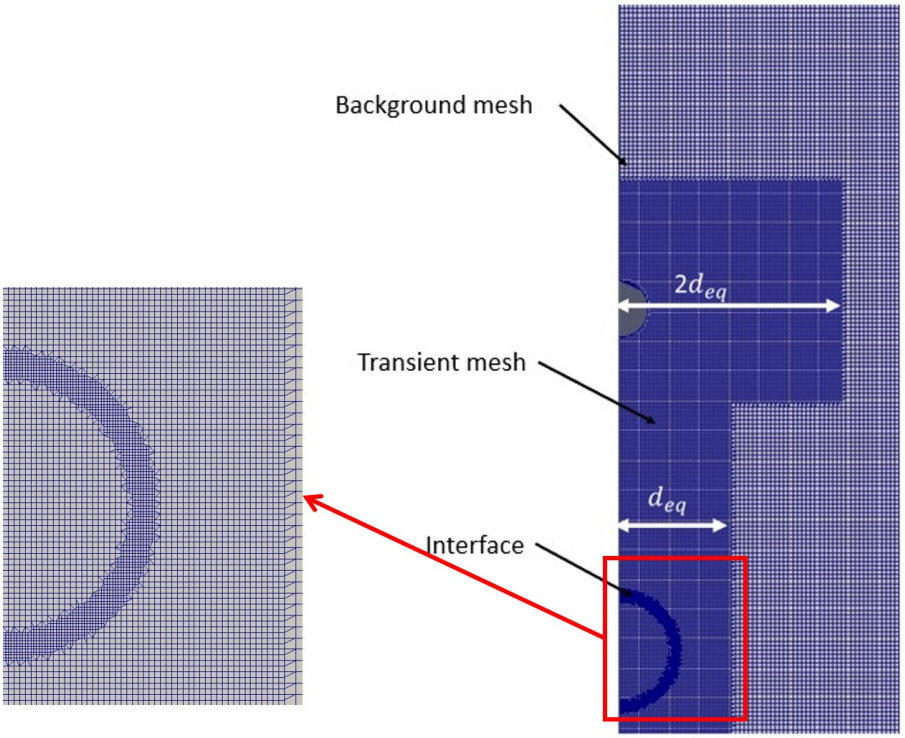

Figure 4.11: Domain descretizition at $t = 0$

Since no detailed reference on the bulk fluid refinement can be found, a static transient region with intermediate refinement level is inserted in the domain, which includes all the space where refinement is potentially necessary. Figure 4.11 shows the descretization of the domain in initial state. The refinement of the domain can be divided into three refinement levels: the background mesh with mesh cell spacing $h = \frac{1}{25}d_{\text{eq}}$ of refinement level 0; the transitional region with= $h = \frac{1}{50}d_{\text{eq}}$ of refinement level 1; the adaptive refinement for interface with $h = \frac{1}{100}d_{\text{eq}}$ of refinement level 2, where $Cn = 0.01$ and $N_{\text{di}} = 4$ is valid. Note that only the refinement on the interface of level 3 is adaptive and moves with the rising motion of the bubble. The domain under this discretization strategy contains approximately 1.5×10^6 cells.

4.3.2 Validation of Adaptive Mesh Refinement

The terminal state of 3D simulation will be compared with the free rising simulation to validate the AMR method.Figure 4.12 compares the velocity profile of the 3D simulation with AMR and the axisymmetric simulation of free rising. The evolution of bubble velocity can be divided into three stages: in the first stage the bubble obtains the most of the acceleration in a very short period; the bubbles accelerates mush slower in the second stage and reach the terminal state and finally, decelerates due to the cylinder in the third part. The two curves are almost identical from the initial state to $t = 0.03$ s. In this process the bubble undergoes the most of the acceleration. The two curves show small deviation from $t = 0.03$ s to $t = 0.1$ s, where the terminal is assumed to be obtained. The velocity calculated by 3D simulation is overall slightly larger than the reference and fluctuation on the curve obtained by 3D simulation can also observed. The most probable reason of this deviation lies in the mesh refinement method: the region of bulk fluid that is very close to the interface needs further refinement. A quantitative instigation on the optimization may be done in the future.

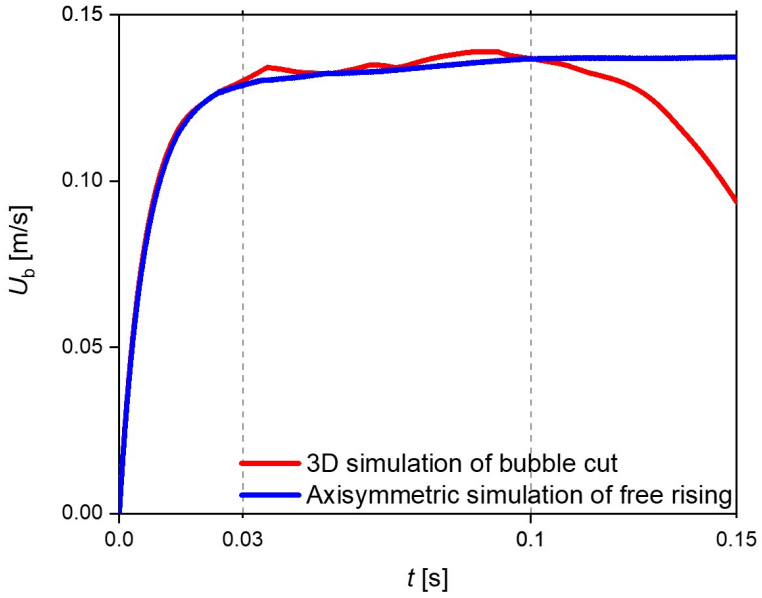

Figure 4.12: Bubble velocity evolution until the terminal state

AMR is proved to impose even smaller influence on the terminal shape of the bubble, which is essential for the further deformation by the cut. Figure 4.13 shows the shape of bubble in the 3D simulation at $t = 0.1s$. The height and the width of the bubble are almost identical to the bubble shown in figure 4.4.

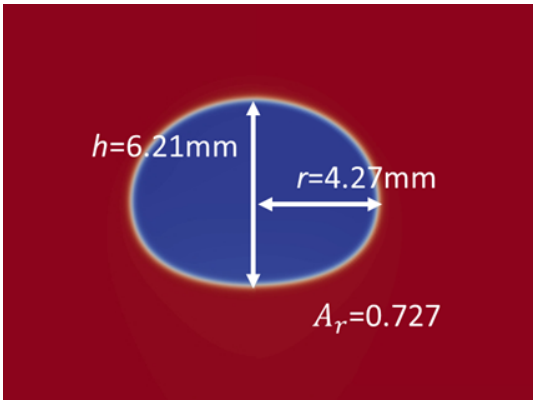

Figure 4.13: Bubble of shape of terminal state of 3D simulation at $t = 0.1s$

4.3.3 Results and Discussion of 3D Bubble Cutting

Before further discussion of the simulation results, it should be noticed that the temperature of experiment varies in20 °C to 22.5 °C whereas the physical properties applied in simulations in this section is calculated under the assumption that the temperature is 20 °C. Since then there might be small deviation between the experiment and the simulation result.

Global Deformation during Bubble Cutting

The previous simulation in planar domain fails to give very exact description of shape of the bubble by interaction with the solid cylinder whereas the planar simulation of bubble slip-over shows much better accordance with the experiment. A potential reason to explain this difference lies in the fact that there is no fundamental change of the bubble shape by slip-over. The bubble shape in the cutting process, however, undergoes significant deformation in the middle, where a narrow "neck" can be observed the break up the mother bubble. This deformation is believed not only in the plane that is perpendicular to the cylinder axis. Deformation in the direction of cylinder axis, which is neglected in the planar simulation, is taken into consideration in the 3D simulation and can be observed in different directions.

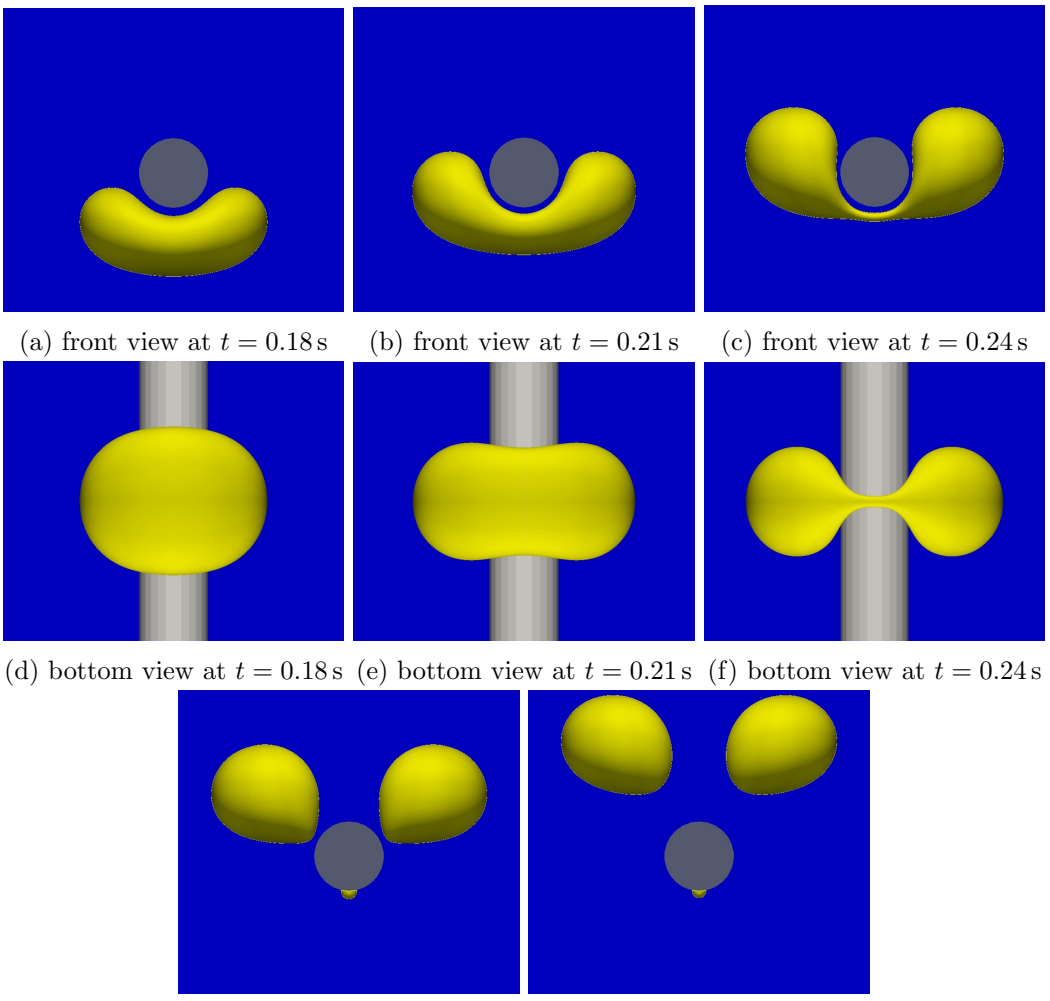

(a) front view at $t = 0.18\,\mathrm{s}$ (b) front view at $t = 0.21\,\mathrm{s}$ (c) front view at $t = 0.24\,\mathrm{s}$

(d) bottom view at $t = 0.18\,\mathrm{s}$ (e) bottom view at $t = 0.21\,\mathrm{s}$ (f) bottom view at $t = 0.24\,\mathrm{s}$

(g) front view at $t = 0.27\,\mathrm{s}$ (h) front view at$t = 0.30\,\mathrm{s}$

Figure 4.14: Interface evolution during the bubble cutting process for $d_{\mathrm{eq}} = 7.8\,\mathrm{mm}$

Figure 4.14 shows the 3D evolution of the interface during the process of cut. The shape of the bubble shows better match with the experiment result than the 2D simulation in front view shown in figure 4.14a, 4.14b and 4.14c. Two major improvements can be seen here: deformation of the bubble before contact with the solid cylinder is well in accordance with the experiment instead of the over-extension observed in 2D simulation: the bottom of the bubble shows a bending profile whereas bubble in planar domain shows a flat profile. The generation and evolution of the narrow connection at the bottom of the cylinder can be better observed in bottom view shown in figure 4.14d, 4.14e and 4.14f. the figures show

that the bubble shrinks not only in the direction of height but also in the direction of cylinder axis at the same time. The bubble extends laterally and shrinks uniformly in the direction of the cylinder before the contact (shown in figure 4.14d). Further shrink in this direction after the contact with the cylinder can be observed in figures 4.14e and 4.14f, where there is obvious shrink only in the middle of the bubble. The middle of the bubble turns narrow very quickly in two directions. Finally, two daughter bubbles are generated and turns into spherical shape quickly under influence of surface tension.

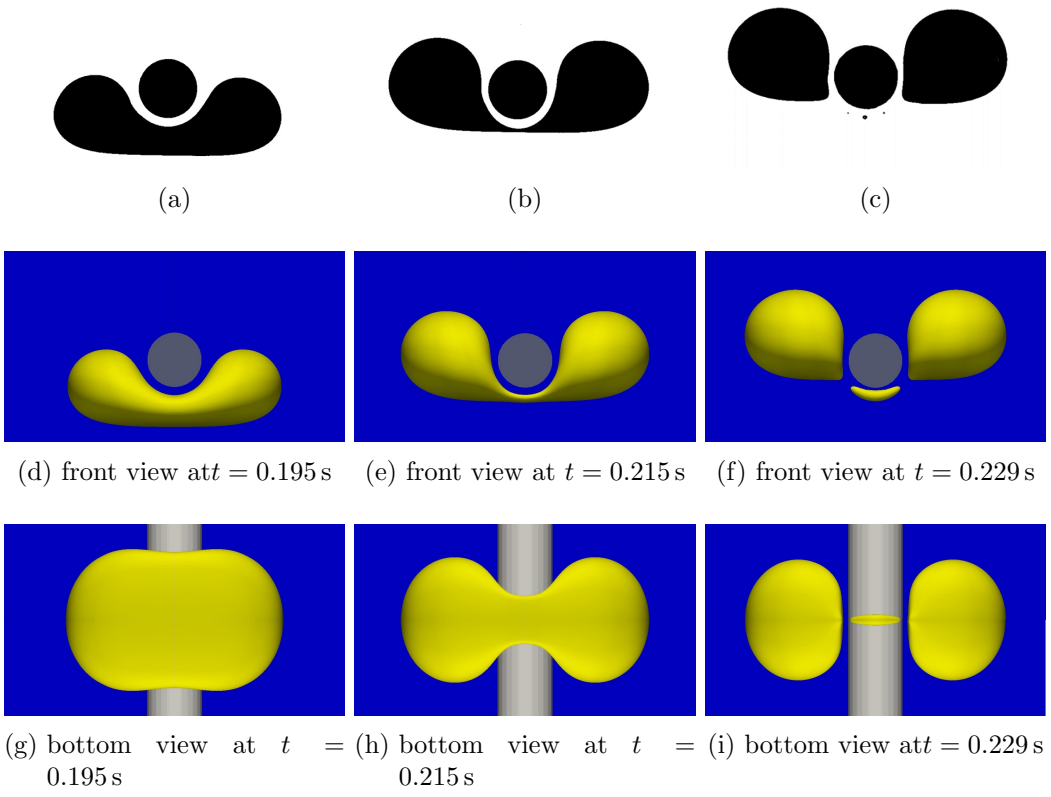

(a) (b) (c)

(d) front view at$t = 0.195\,\mathrm{s}$ (e) front view at $t = 0.215\,\mathrm{s}$ (f) front view at $t = 0.229\,\mathrm{s}$

(g) bottom view at $t = 0.195\,\mathrm{s}$ (h) bottom view at $t = 0.215\,\mathrm{s}$ (i) bottom view at$t = 0.229\,\mathrm{s}$

Figure 4.15: Comparison of bubble deformation of bubble cut, $d_{\mathrm{eq}} = 9.85\,\mathrm{mm}$. (a)-(c): bubble shape evolution in experiment[30]. (d)-(f): bubble interface by *phaseFieldFoam*, front view; (d)-(f): bubble interface by *phaseFieldFoam*, bottom view.

Similar evolution process can also be observed by he cutting of larger bubble with $d_{\mathrm{eq}} = 9.85\,\mathrm{mm}$ by the cylinder with same diameter and same contact angle of 60°. Numerical parameters in this simulations are investigated section 4.1 This phenomena is investigated with the same numerical approach. The behavior of the interface by the cutting is compared with the experiment result in figure 4.15. The shape of the bubble is well in accordance with the experiment. Compared with the smaller bubble, the larger bubble undergoes stronger in axisymmetric deformation due to higher Eötvos number before the contact(figure 4.15d and 4.15g). The behavior by the cutting is the very similar: the bubble bubble shrinks quickly in the middle whereas no significant deforamion can observed on the left and right side.

In both cases the cylinder is completely wetted. According to the conclusion obtained in section 4.2, the behavior of bubbles will not be affected by the wettability of the cylinder surface for the both investigated cases.

Liquid Film Thickness and Wettability

The 3D simulation provides also better prediction of the liquid film, which is prerequisites of the irrelevance of the wettabilty the cylinder surface. It should be noticed that the liquid thicknessd is uniformly distributed around the cylinder surface. The shortest distance from the bubble to the bottom of the cylinder by the cutting d_{F} is selected as the symbol of the liquid thickness to be compared quantitatively (shown in figure 4.16).

Figure 4.16: Liquid film thickness measurement method [30]

Figure 4.19 compares the liquid film thickness measured in experiment by Rohlfs [30] and the result of *phaseFieldFoam*. The thickness of the liquid film in the numerical thesis slightly smaller than the experiment result. This deviation is acceptable, considering the fact of the fluctuation of experiment temperature and measurement error. Since then the simulation is proved to be able to give a correct description of liquid film.

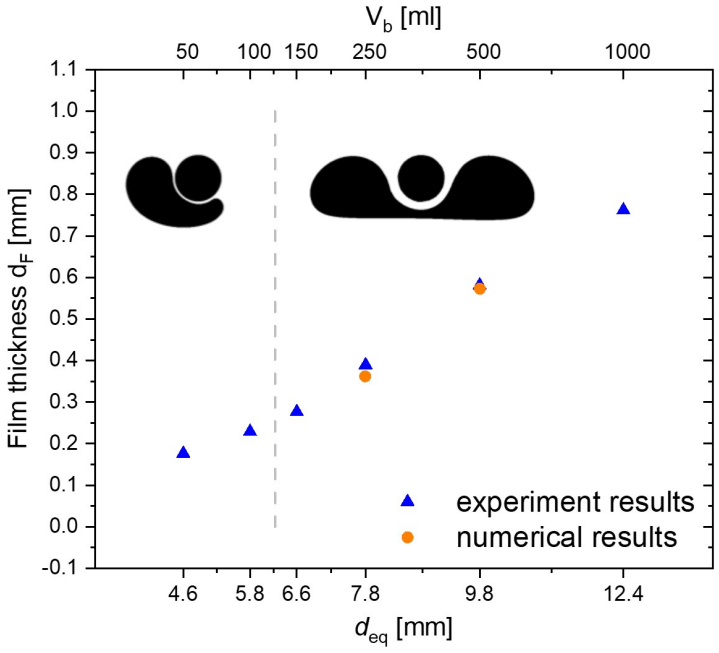

Figure 4.17: Comparison of liquid film thickness of experiment [30] and numerical simulation, $d_{\mathrm{cylinder}} = 4\,\mathrm{mm}$.

The irrelevance of wettability can be explained by means of phase field method. Figure 4.18 shows the profile of order parameter C in the process of bubble cutting. It can be observed that the diffusion region is thinner than the liquid film and as a result, the

order parameter is uniformly 1 on the cylinder surface. According to the mathematical description of wetting condition given in equation (2.16), the term includes contact angle is 0 from the boundary on the solid surface.

The liquid film share the same order of magnitude of 10^{-1} mm and the current applied interface thickness is of order of magnitude 1×10^{-2} mm. This currently applied interface is thin enough able to isolate the cylinder surface from the influence of diffusion region and obviously the influence of wettebility will not be observed in simulations with thinner interface that is nearer to the sharp edge as in reality. With the discussion above, the result of this simulation in this thesis supports the conclusion that wettablity does not affect the behavior of bubble cutting.

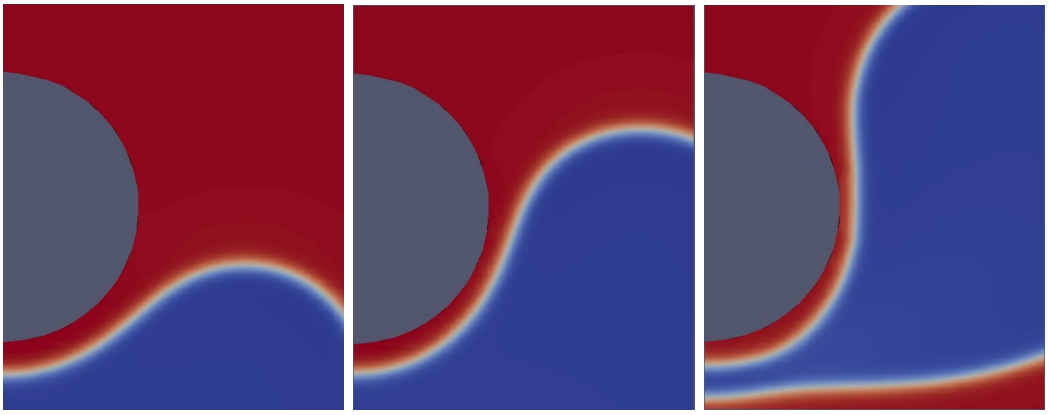

(a) $t = 0.18s$ (b) $t = 0.21s$ (c) $t = 0.24s$

Figure 4.18: Distribution of order parameter of near the cylinder with contact angle $\theta = 60°$, $d_{\text{eq}} = 7.8\,\text{mm}$

Discussion of Satellite Bubble

The major difference between the 3D simulation and the experiment result lies in the behavior of satellite bubble. According to the experiment [30], no obvious satellite bubble can be observed for $d_{\text{eq}} = 7.8\,\text{mm}$ and multiple satellite bubbles can seen for $d_{\text{eq}} = 9.85\,\text{mm}$. However, the result of *phaseFieldFoam* share very similar mechanism of the generation of satellite bubbles for the both cases. The simulation result of *phaseFieldFoam* shows that the satellite bubble is generated from the gas phase under the cylinder that is in thread shape. Similar gas thread can also be observed in the experiment where satellite is generated. Figure 4.17 shows this gas thread in Rohlfs' experiment[30], in which case a larger bubble is investigated. This deviation is believed to be due to the limit of intrface thickness applied in the current simulation. However, gas thread in the reality is much thinner than the liquid film whereas the gas thread in the simulation result share the same thickness with the liquid film. Experience shows that the interface thickness is supposed to be or smaller than 1/10 of characteristic length of the investigated single phase in phase field method to grantee the approach of sharp edge hypothesis. Since the interface is in the order of magnitude of $10^{-2}\,\text{mm}$, gas thread thickness that is smaller than $10^{-1}\,\text{mm}$ will not be correctly calculated. Figure 4.20 with the detailed evolution of the gas thread proves this reasoning: the decrease of distance of two interfaces leads to the overlap of the diffusion region; the overlapped area increases until the threshold is reached, after which the fusion of interface will happen. Since then any gas thread that is thinner than this threshold cannot stably exist.

Figure 4.19: Generation of satellite bubble in experiment [30], $d_{\text{eq}} = 9.5\text{mm}$

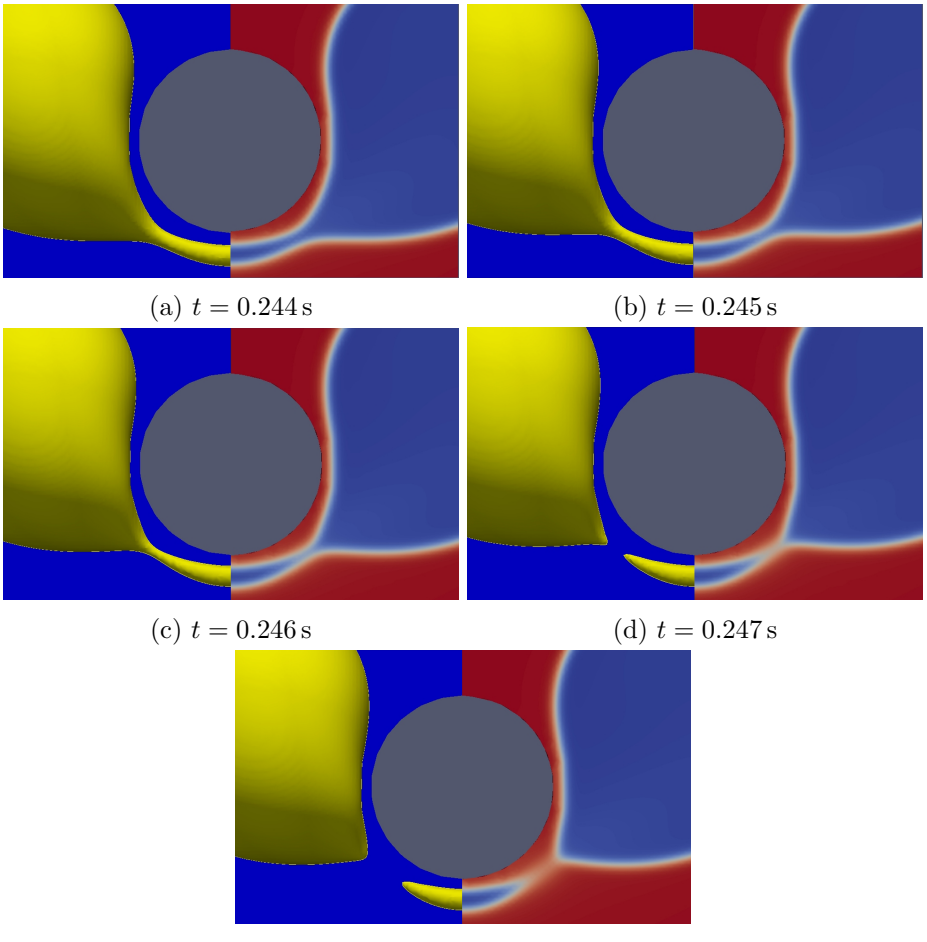

(a) $t = 0.244\,\text{s}$ (b) $t = 0.245\,\text{s}$

(c) $t = 0.246\,\text{s}$ (d) $t = 0.247\,\text{s}$

(e) $t = 0.248\,\text{s}$

Figure 4.20: Generation of satellite bubble of $d_{\text{eq}} = 7.8\text{mm}$ in *phaseFieldFoam*, left part of the picture is the interface; the right part is the order parameter distribution

,

For more precise description of the generation of satellite bubbles, much more thinner interface must be applied. This refinement is, however, limited by the absence of the characteristic length derived from the satellite bubbles. Furthermore, the prediction of

satellite bubbles is very challenging considering the calculation cost in 3D simulation.

5. Summary and Outlook

This thesis presents numerical studies on the interaction of a bubble and a horizontal cylinder. This phenomena is very common in multi-phase reactors. The main purpose of the study is to validate phase field method and obtain comprehensive understanding of underlying physics that governs the behavior of bubbles during the cutting by a horizontal cylinder and clarifies the deviation on the influence of wettability between previous experiment and numerical investigations. To increase the calculation efficiency adaptive mesh refinement is used and validated.

The phase-field method based solver *phaseFieldFoam* is validated through comparison with benchmark result for bubble free-rising problem in planar domain. The velocity evolution and terminal shape are compared. Influence of numerical parameters Cn, N_{di} and mobility pre-factor χ is investigated. Both the dynamic velocity evolution and terminal shape is consistent with benchmark.

After the validations, the cutting behavior of single bubble and horizontal cylinder is investigated. Axi-symmetric simulations for free bubble rising are performed to determine the numerical configurations for the following simulations and domain height which is essential for the following 3D simulation. The velocity evolution and terminal shape also serve as reference for the valuation of adaptive refinement. Simulation of bubble cut is performed in planar domain to gain preliminary knowledge of different possibilities of the interactions between the bubble and cylinder. Two different bubble diameter, $d_{\mathrm{eq}} = 4.57\,\mathrm{mm}$ and $d_{\mathrm{eq}} = 7.8\,\mathrm{mm}$ are selected according to previous investigation. The results are compared with and qualitatively consistent with experiment results. The bubble with $d_{\mathbf{eq}} = 4.57\,\mathrm{mm}$ slips over the cylinder from one side and keeps intact. The shape of the bubble with matches the experiment result very well due to light deformation. The bubble with $d_{\mathrm{eq}} = 7.8\,\mathrm{mm}$ is cut into two daughter bubbles by the cylinder. Obvious deviation of bubble shape can be observed because of the intensive deformation that is neglected in the planar simulation. Influence of wettability is investigated by imposing different boundary conditions on the cylinder surface. The bubble behavior by contact angles 60°, 90° and 120° are identical. The reason is liquid film isolates the bubble from the cylinder and thus contact line where wettability is usually considered does not exists.

Adaptive mesh refinement is made on background mesh with low resolution for 3D simulation of bubble cutting. Order parameter C is selected as the control parameter of adaptive mesh refinement. The other refinement configurations, for example, the refinement level,

refinement upper and lower limit and refinement frequency is considered and optimized. Since the adaptive refinement is currently limited to the interface region, further refinement is added in space where the flow of liquid may affect the behavior of the bubble. This region of transitional refinement is static and thus covers a large domain. A better solution would be, that the transitional refinement is made also adaptively and possibly controlled by the velocity of the bubble instead of order parameter. The discretization is validated by velocity evolution of bubble free rising and terminal shape obtained in the axisymmetric simulation. The terminal velocity and bubble shape is consistent with the reference obtained in simulation of free bubble rising . The velocity evolution differs from the reference slightly. A possible reason is the current discretization method is still not able to capture all the flow structures around the interface perfectly. It is also possible that the numerical parameters of Cahn Hilliard method require further optimization when adaptive refinement is applied.

The 3D simulation is performed for two bubble diameters, namely $d_{\mathrm{eq}} = 7.8\,\mathrm{mm}$ and $d_{\mathrm{eq}} = 9.85\,\mathrm{mm}$. The bubble shape evolution is consistent with the experiment. Intensive 3D deformation is observed at the bottom of the bubble. In both cases, the solid cylinder is completely wetted. The liquid film thickness is compared with the experiment result and it is consistent with the experiment data. Detailed distribution of order parameter is shown to explain the irrelevance of wettability. All the discussion validates the conclusion of the experiment. It should be noted here that the conclusion is only valid for perfect smooth cylinder, in which case the liquid film thickness is overall uniform. In the industrial application, roughness of the cylinder surface will lead to local increase or decrease of the liquid film thickness and thus to partial wetting of the solid surface. Furthermore, the wire mesh in multi-phase reactor may be not necessarily perfect cylinder. The cutting behavior on wire mesh of other shape is still to be investigated.

The largest deviation between the numerical simulation and experiment is the generation of satellite bubble(s). The numerical simulation fails to predict the behavior of satellite bubble correctly. The reason lies in the thickness of diffusion interface. Process of fusion of two interface is discussed for better understanding the problem. Very thin interface thickness ϵ is needed to calculate the behavior of satellite bubble precisely and this brings at the same time high requirement of discretization which is limited by both numerical scheme and calculation resources.

Symbols and Abbreviations

Latin Symbols

A_r	[-]	aspect ratio
Bo	[-]	Bond number
C	[-]	order parameter
Cn	[-]	Cahn number
d_{eq}	[m]	equivalent diameter
Eo	[-]	Eötvös number
F	[J]	free energy
F_{B}	[J]	buoyancy force
h	[m]	mesh spacing
L	[m]	reference length
L_{di}	[m]	interface thickness
Mo	[-]	Morton number
N_{di}	[-]	number of mesh cells per interface thickness
p	[N/m^2]	pressure
Re	[-]	Reynolds number
t	[s]	time
t^*	[-]	dimensionless time
u	[m/s]	velocity
u^*	[-]	dimensionless velocity
We	[-]	Weber number

Greek Symbols

γ_{LV}	[N/m]	liquid-gas interfacial tension
γ_{SV}	[N/m]	solid-gas interfacial tension
γ_{SL}	[N/m]	liquid-solid interfacial tension
ϵ	[m]	capillary width
θ	[°]	contact angle
κ	[m$^3 \cdot$ s/kg]	Cahn Hilliard mobility
λ	[J/m]	mixing energy parameter
μ	[kg/(m $\cdot$ s)]	dynamic viscosity
ρ	[kg/m^3]	density
σ	[N/m]	surface tension
ϕ	[J/m^3]	Cahn-Hilliard chemical potential

Subscript

B	bubble
g	gravitation
G	gas phase
L	liquid phase
max	maximal
n	neutral surface

Abbreviation

2D	Two Dimensional
3D	Three Dimensional
AMR	Adaptive Mesh Refinement
CFD	Computational Fluid Dynamics
CH	Cahn Hilliard
OpenFOAM	Open Source Field Operation And Manipulation
VOF	Finite-Volume Method

List of Figures

List of Tables

Bibliography

[1] S. Aoyama, K. Hayashi, S. Hosokawa, and A. Tomiyama. Shapes of ellipsoidal bubbles in infinite stagnant liquids. *International Journal of Multiphase Flow*, 79:23 – 30, 2016.

[2] M. W. Baltussen, J. A. M. Kuipers, and N. G. Deen. A numerical study of cutting bubbles with a wire mesh. *Chemical Engineering Science*, 165:25 – 32, 2017.

[3] D. Bonn, J. Eggers, J. Indekeu, J. Meunier, and E. Rolley. Wetting and spreading. *Rev. Mod. Phys.*, 81:739–805, May 2009.

[4] A. J. Bray. Theory of phase-ordering kinetics. *Advances in Physics*, 51(2):481–587, 2002.

[5] J. W. Cahn and John E. Hilliard. Free energy of a nonuniform system. iii. nucleation in a two-component incompressible fluid. *The Journal of Chemical Physics*, 31(3):688–699, 1959.

[6] John W. Cahn. Free energy of a nonuniform system. ii. thermodynamic basis. *The Journal of Chemical Physics*, 30(5):1121–1124, 1959.

[7] John W. Cahn and John E. Hilliard. Free energy of a nonuniform system. i. interfacial free energy. *The Journal of Chemical Physics*, 28(2):258–267, 1958.

[8] X. Cai, M. Wörner, H. Marschall, and O. Deutschmann. Numerical study on the wettability dependent interaction of a rising bubble with a periodic open cellular structure. *Catalysis Today*, 273:151 – 160, 2016.

[9] Hector D. Ceniceros, Rudimar L. Nós, and Alexandre M. Roma. Three-dimensional, fully adaptive simulations of phase-field fluid models. *Journal of Computational Physics*, 229(17):6135 – 6155, 2010.

[10] Y. Chen and J.Shen. Efficient, adaptive energy stable schemes for the incompressible cahn–hilliard navier–stokes phase-field models. *Journal of Computational Physics*, 308:40 – 56, 2016.

[11] N. S. Cheng. Formula for the viscosity of a glycerol-water mixture. *Industrial and Engineering Chemistry Research*, 47(9):3285–3288, 2008.

[12] P. Gilles de Gennes, Françoise B. Wyart, and D. Quéré. *Capillarity and Gravity*, pages 33–67. Springer New York, New York, NY, 2004.

[13] W. Dijkhuizen, I. Roghair, M. Van Sint Annaland, and J.A.M. Kuipers. Dns of gas bubbles behaviour using an improved 3d front tracking model—drag force on isolated bubbles and comparison with experiments. *Chemical Engineering Science*, 65(4):1415 – 1426, 2010.

[14] H. Ding, E. Q. Li, F. H. Zhang, Y. Sui, P. D. M. Spelt and, and S. T. Thoroddsen. Propagation of capillary waves and ejection of small droplets in rapid droplet spreading. *Journal of Fluid Mechanics*, 697:92–114, 2012.

[15] M. P. Dudukovic, F. Larachi, and P. L. Mills. Multiphase reactors – revisited. *Chemical Engineering Science*, 54(13):1975 – 1995, 1999.

[16] W. L. Haberman and R. K. Morton. An experimental investigation of the drag and shape of air bubbles rising in various liquid. *American Documentation*, 7(3)(188-200), 1953.

[17] V. Höller, K. Radevik, L. Kiwi-Minsker, and A. Renken. Bubble columns staged with structured fibrous catalytic layers: Residence time distribution and mass transfer. *Industrial & Engineering Chemistry Research*, 40(6):1575–1579, 2001.

[18] D. Jacqmin. Calculation of two-phase navier–stokes flows using phase-field modeling. *Journal of Computational Physics*, 155(1):96 – 127, 1999.

[19] D. Jacqmin. Contact-line dynamics of a diffuse fluid interface. *Journal of Fluid Mechanics*, 402:57–88, 2000.

[20] B. Bhushan K. Koch and W. Barthlott. Diversity of structure, morphology and wetting of plant surfaces. *Soft Matter*, 4:1943 – 1963, 2008.

[21] M. Klumpp, A. Inayat, J. Schwerdtfeger, C. Körner, R.F. Singer, H. Freund, and W. Schwieger. Periodic open cellular structures with ideal cubic cell geometry: Effect of porosity and cell orientation on pressure drop behavior. *Chemical Engineering Journal*, 242:364 – 378, 2014.

[22] K.Y. Law and H. Zhao. Surface wetting: Characterization, contact angle, and fundamentals. *MRS Bulletin*, 41(8):635–635, 2016.

[23] H. J. Lee and S. Michielsen. Lotus effect: Superhydrophobicity. *The Journal of The Textile Institute*, 97(5):455–462, 2006.

[24] L. Liu, H.J. Yan, G. J. Zhao, and J. C. Zhuang. Experimental studies on the terminal velocity of air bubbles in water and glycerol aqueous solution. *Experimental Thermal and Fluid Science*, 78:254 – 265, 2016.

[25] N. Moelans, B. Blanpain, and P. Wollants. An introduction to phase-field modeling of microstructure evolution. *Calphad*, 32(2):268 – 294, 2008.

[26] N. Nikolopoulos, A. Theodorakakos, and G. Bergeles. Three-dimensional numerical investigation of a droplet impinging normally onto a wall film. *Journal of Computational Physics*, 225(1):322 – 341, 2007.

[27] K. Pangarkar, T. J. Schildhauer, J. Ruud van Ommen, J. A. Moulijn, and F. Kapteijn. Experimental and numerical comparison of structured packings with a randomly packed bed reactor for fischer–tropsch synthesis. *Catalysis Today*, 147:S2 – S9, 2009. 3rd International Conference on Structured Catalysts and Reactors, ICOSCAR-3, Ischia, Italy, 27-30 September 2009.

[28] S. H. Park, C. Park, J. Y. Lee, and B.Lee. A simple parameterization for the rising velocity of bubbles in a liquid pool. *Nuclear Engineering and Technology*, 49(4):692 – 699, 2017.

[29] R. Clift, J. R. Grace, and M. E. Weber. *Bubbles, drops and particles.* Acad.Press, 3rd. printed edition, 1995.

[30] P. Rohlfs. *Einfluss des Benetzungsverhaltens auf die Blasenzerteilung an einem Zylinder.* Bachelor thesis, Karlsruher Institute of Technology, 2018.

[31] S. Hosseini, S. Turek, and C. Palmes. Isogeometric analysis of the navier–stokes–cahn–hilliard equations with application to incompressible two-phase flows. *J. Comput. Phys*, 348:171–194, 2017.

[32] E. Burman, S. Ganesan S. Hysing, S. Turek, D. Kuzmin, N. Parolini and L. Tobiska. Quantitative benchmark computations of two-dimensional bubble dynamics. *Int. J. Numer. Meth. Fluids*, 25:1259–1288, 2009.

[33] Q. I. E. Segers. *Cutting bubbles using wire-mesh structures : direct numerical simulations*. PhD thesis, Department of Chemical Engineering and Chemistry, 2015.

[34] R. Tadmor. Line energy and the relation between advancing, receding and young contact angles. *Langmuir*, 20 (18):7659 – 7664, 2004.

[35] K. Takamura, H. Fischer, and Norman R. Morrow. Physical properties of aqueous glycerol solutions. *Journal of Petroleum Science and Engineering*, 98-99:50 – 60, 2012.

[36] A. Theodorakakosand and G. Bergeles. Simulation of sharp gas–liquid interface using vof method and adaptive grid local refinement around the interface. *International Journal for Numerical Methods in Fluids*, 45:421 – 439, 06 2004.

[37] W. Villanueva and G. Amberg. Some generic capillary-driven flows. *International Journal of Multiphase Flow*, 32(9):1072 – 1086, 2006.

[38] Y. C. Wu. *Numerical Simulation of Droplet Impact and Rebound on a Wall*. Master thesis, Karlsruhe Institute of Technology, 2017.

[39] X.Cai. *Interface-Resolving Simulations of Gas-Liquid Two-Phase Flows in Solid Structures of Different Wettability*. PhD thesis, Karlsruher Institut für Technologie (KIT), 2016.

[40] T. Young. An essay on the cohesion of fluids. *Philosiphical Transactions of the Royal Society of London*, 95:85–67, 1805.

[41] Z. Yu and L. S. Fan. An interaction potential based lattice boltzmann method with adaptive mesh refinement (amr) for two-phase flow simulation. *Journal of Computational Physics*, 228(17):6456 – 6478, 2009.

[42] P. Yue and J. J. Feng. Can diffuse-interface models quantitatively describe moving contact lines? *The European Physical Journal Special Topics*, 197(1):37, Aug 2011.

[43] P. Yue, C. Zhou, and J. J. Feng. Sharp-interface limit of the cahn–hilliard model for moving contact lines. *Journal of Fluid Mechanics*, 645:279–294, 2010.

[44] P. T. Yue, James J. Feng, C. Liu, and J. Shen. A diffuse-interface method for simulating two-phase flows of complex fluids. *Journal of Fluid Mechanics*, 515:293–317, 2004.